Swiss Journal of Palaeontology

RESEARCH Open Access

Osteology and histology of a *Plateosaurus trossingensis* (Dinosauria: Sauropodomorpha) from the Upper Triassic of Switzerland with an advanced chronic pathology

Sina F. J. Dupuis[1], Jordan Bestwick[1], Dennis M. Hansen[2], Esben Horn[3], Stacey Wiik[3], Rasmus Frederiksen[3], Robert Zboray[4,5], Kiarash Tajbakhsh[4,6], Ursina Bachmann[7], Ben Pabst[8] and Torsten M. Scheyer[1*]

Abstract

The sauropodomorph *Plateosaurus* is one of the best-known dinosaurs from Europe due to the large numbers of articulated skeletons discovered from bonebed horizons in Switzerland and Germany. *Plateosaurus* exhibits high degrees of developmental plasticity, which makes investigations of specimen life-histories from gross morphology alone difficult. Furthermore, comparatively few specimens have been rigorously examined for possessing any evidence of pathology, i.e., injury or disease, that could provide insight into how these dinosaurs lived. Here, we provide an osteological description of a nearly complete *Plateosaurus trossingensis* (excavation ID SMF 18.1, collection NMZ 1000001) from the Late Triassic Klettgau Formation from Frick, Switzerland, with an unusual pathology in its right scapula and proximal portion of the right humerus. We also perform histological analyses on two dorsal ribs to investigate the relative ontogenetic stage and life history of the specimen and investigate the morphology and aetiology of its scapula-humerus pathology using Micro-Computed Tomography and comparisons with a previously undescribed *Plateosaurus* from Frick (SMF 11.4; comprising left and right radii and ulnae) that exhibits pathological tissues. We infer that NMZ 1000001 was an adult of around 23–25 years of age when it died. We estimate a total body length of around 7.7 m, making NMZ 1000001 one of the largest known specimens from Frick and an above average-sized adult for the species overall. The scapula-humerus pathology is characterised by highly rugose surface textures, possible element fusion and extensive remodelling of internal bone structures. We infer the pathology to be a chronic case of osteomyelitis (bone tissue infection). Based on the size and extent of the infected area it is likely one of most advanced cases known from the fossil record. We further document the process of producing an exhibit with a museum-grade life reconstruction based on the pathological fossil.

Keywords Sauropodomorph, *Plateosaurus*, Frick, Klettgau Formation, Osteology, Computed tomography, Pathology, Histology, Osteomyelitis, Museum exhibit

Handling editor: Nicole Klein

*Correspondence:
Torsten M. Scheyer
tscheyer@pim.uzh.ch
Full list of author information is available at the end of the article

Introduction

The non-sauropod sauropodomorph *Plateosaurus* (Meyer, 1837) is one of the earliest discovered and best-known dinosaurs from the Late Triassic of Europe (Moser, 2003; Sander, 1992). The genus has had a complicated taxonomic history (see Regalado Fernández et al. 2023 and Schaeffer 2024 for reviews), and three species are tentatively currently recognised: the type species, *P. trossingensis* (Fraas, 1913; ICZN, 2019), *P. gracilis* (Jaekel, 1914), and *P. longiceps* (Huene, 1907). However, taxonomic contention surrounding the genus remains, such as whether *P. longiceps* is actually distinct from *P. trossingensis* and whether *P. trossingensis* is truly equivalent to the original type species *P. engelhardti*, now a nomen dubium (Galton & Kermack, 2010; Galton, 2012, 2013; Lallensack et al., 2021).

Plateosaurus is known from numerous, relatively complete skeletons from horizons across Europe (Jaekel, 1914; Huene, 1928; Seemann, 1933), with the three best localities with regards to both specimen numbers and preservation quality being Frick in northern Switzerland, and Trossingen and Halberstadt in Germany (Sander, 1992). Of these localities, both Frick and Trossingen are actively studied today (Schoch & Seegis, 2014; Lallensack et al., 2021; Schaeffer et al., 2023; Mujal et al., 2024). Frick, Trossingen and Halberstadt are often informally referred to as *Plateosaurus* bonebeds. Skeletons from these bonebeds are typically preserved in very similar postures—laying on their abdomens with twisted anterior trunks and recurved tails. The forelimbs are often sprawled laterally and point posteriorly, while the hindlimbs are preserved in crouching positions with bent knee- and ankle joints. This orientation, informally known as the "frog-kick" posture, is characteristic of the mud miring hypothesis, in which large *Plateosaurus* individuals become trapped in mudholes on palaeo-floodplains and unsuccessfully use their limbs to try to pull themselves out (Seemann, 1933; Sander, 1992; Schoch, 2011; Schoch & Seegis, 2014).

Specimens from these bonebeds have led to a wealth of understanding of *Plateosaurus* life-histories. For example, *Plateosaurus* exhibits large variation in body size, with adults measuring between 4.8 m and 10 m (Klein & Sander, 2007; Lefebvre et al., 2020; Nau, 2022). The size range is somewhat location-specific, with Frick specimens being, on average, smaller than Trossingen and Halberstadt individuals (Klein & Sander, 2007; Nau, 2022). Furthermore, *Plateosaurus* exhibits a high degree of developmental plasticity, with estimates for reaching skeletal maturity between 11 and 21 years of age (based on histological analyses and growth curve modelling; Sander & Klein, 2005; Klein & Sander, 2007; Griebeler et al., 2013). These findings show that regardless of the abundance of bonebed specimens, every individual is important for understanding the complexity and evolution of growth strategies in *Plateosaurus* and sauropodomorphs in general.

Despite this abundance of material, there is a paucity of information concerning palaeopathologies—the study of injuries and diseases from the fossil record—in this sauropodomorph. Investigating osteological pathologies, including describing the morphology of affected tissues and constraining its aetiology in extinct taxa, can reveal much about their behaviour, life history, interspecific interactions (e.g., predator–prey relationships), and interactions with the environments in which they lived (Annè et al., 2015; Foth et al., 2015; Hamm et al., 2020; Hanna, 2002; Rothschild & Storrs, 2003; Rothschild et al., 2003; Schaeffer et al., 2024; Xing et al., 2018). The only pathologies that have been described in *Plateosaurus* specimens are trauma-related injuries of caudal vertebrae chevrons (Schaeffer et al., 2024). However, no other types of pathology have been identified from this sauropodomorph, nor from any other part of the body besides the tail.

Here, we provide a detailed study of a nearly complete, articulated specimen of a *Plateosaurus trossingensis* from Frick (excavation ID: Sauriermuseum Frick, SMF 18.1, collection ID: Natural History Museum of the University of Zurich NMZ 1000001, nicknamed 'Teoplati'). This specimen is of scientific interest for several reasons: (i) the specimen is unusually large for the locality; (ii) it exhibits several pathologies across its body, most notably a large morphological deformation on its right scapula and upper right humerus; (iii) the preserved parts of the specimen are largely articulated. We therefore provide a complete osteological description of the specimen, as well as investigations into its possible life-history and distinctive pathologies, including the morphology and aetiology of the latter. Our investigations include comparisons with a currently undescribed *P. trossingensis* specimen from Frick (SMF 11.4; comprising left and right radii and ulnae) that likely exhibits pathological tissues for robust aetiological assessments on the NMZ 1000001 pathology. We also provide a brief account on how the specimen was used to inform (i.e., provide a scientific basis) and create the 'Teoplati' exhibit at the NMZ UZH. This is deemed important considering questions concerning the usefulness of (natural history) museum exhibits, how evidence-based exhibits actually are, and how scientific data are actively communicated and made publicly available to a broader audience beyond academia.

Methods

Geological setting

Specimen NMZ 1000001 was found in 2018 in the 'Upper Part of the Lower Saurian Level' ('Untere Saurierschicht hoch'; Norian, Upper Triassic) of the Gruhalde Quarry in Frick, Canton Aargau, Switzerland (Fig. 1). The lower level mostly comprises carbonate-rich, greyish to variegated marl that contains intraclasts and dolomite lenses (Jordan et al., 2016; Lallensack et al., 2021). The layers are non-continuous and the marl is cut by channels that range from silty marl to coarse-grained sandstone (Fig. 1; Jordan et al., 2016). These deposits are interpreted as overbank deposits of episodic sheet floods in a terrestrial playa environment (Schoch & Seegis, 2014; Jordan et al., 2016; Lallensack et al., 2021).

Specimen history

Specimen NMZ 1000001 comprises a mostly articulated, partial skeleton initially nicknamed "Frosch" ("frog") due to the frog-kick posture in which the skeleton was found (Fig. 2). The body was preserved laying on its abdomen with the anterior trunk twisted to the left and the tail strongly recurved (Fig. 2). The forelimbs are slightly sprawled laterally and point posteriorly, while the hindlimbs are preserved in a crouching position with strong bends in the knee and ankle joints (Fig. 2). It can therefore be assumed that the individual became trapped in a mudhole on the Klettgau floodplain, where it ultimately died after unsuccessfully trying to pull itself out (Seemann, 1933; Sander, 1992; Schoch, 2011; Schoch & Seegis, 2014).

The skull and neck of NMZ 1000001 are lost because quarry activities had accidentally removed the matrix where this part of the skeleton would have been prior to its discovery. After discovery and systematic excavation, the specimen was subsequently divided into smaller blocks and transferred to the Sauriermuseum Aathal (SMA) for further preparation before being transferred to the NMZ UZH for display.

The skeleton is now on display at the NMZ UZH in the original "frog-kick" position (Sander, 1992) (Fig. 2), and is partially embedded in a combination of original and artificial matrix. The display contains the almost complete skeleton, with the important missing elements replaced using casts of other *Plateosaurus* specimens from the Gruhalde Quarry (Fig. 2). The skull is an upscaled version of SMF 16.1 while the entire cervical vertebral series, including the cervical ribs, dorsal vertebrae 1 and 2 and the neural arch of dorsal vertebra 3 are based on casts of specimen SMF 15.1 (Fig. 2). These elements are therefore not included in the osteological description of NMZ 1000001. In addition, the deformed right pectoral girdle is also a cast (Fig. 2) to leave the original elements easily accessible for study. The left humerus was originally found at an angle where only the distalmost third was exposed and the proximal two thirds positioned deeper within the sediment under the rest of the specimen. A cast of the originally exposed portion of the left humerus is therefore on display (Fig. 2) to leave the entire humerus, preserved in two pieces (Fig. S1), accessible for study.

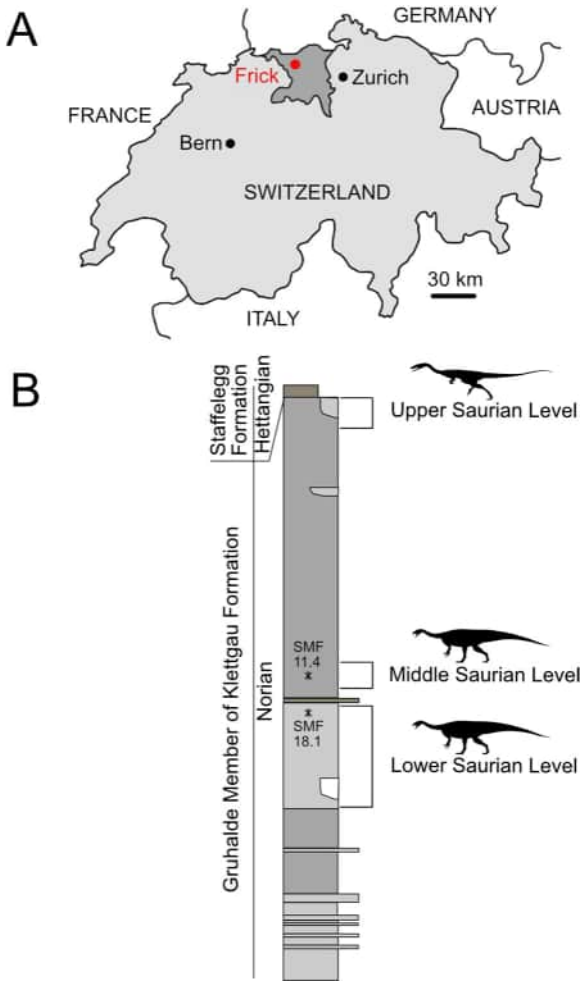

Fig. 1 Stratigraphic and geographic locations of where *Plateosaurus trossingensis* NMZ 1000001 was discovered. **A** Location of Frick in Canton Aargau, northern Switzerland. **B** Stratigraphic section of the Gruhalde Member (Klettgau Formation) exposed at Gruhalde Quarry in Frick, Canton Aargau, showing the approximate section that SMF 18.1 was discovered in. The position of NMZ 1000001 (excavation ID SMF 18.1) and SMF 11.4 are indicated by asterisks. Stratigraphic section redrawn from Jordan et al. (2016). *Plateosaurus trossingensis* silhouette by Scott Hartman from http://www.phylopic.org/ under a Creative Commons Attribution NonCommercial ShareAlike 3.0 Unported license (https://creativecommons.org/licenses/by-nc-sa/3.0/). *Notatesseraeraptor frickensis* silhouette adapted from Zahner and Brinkmann (2019). Silhouettes not to scale

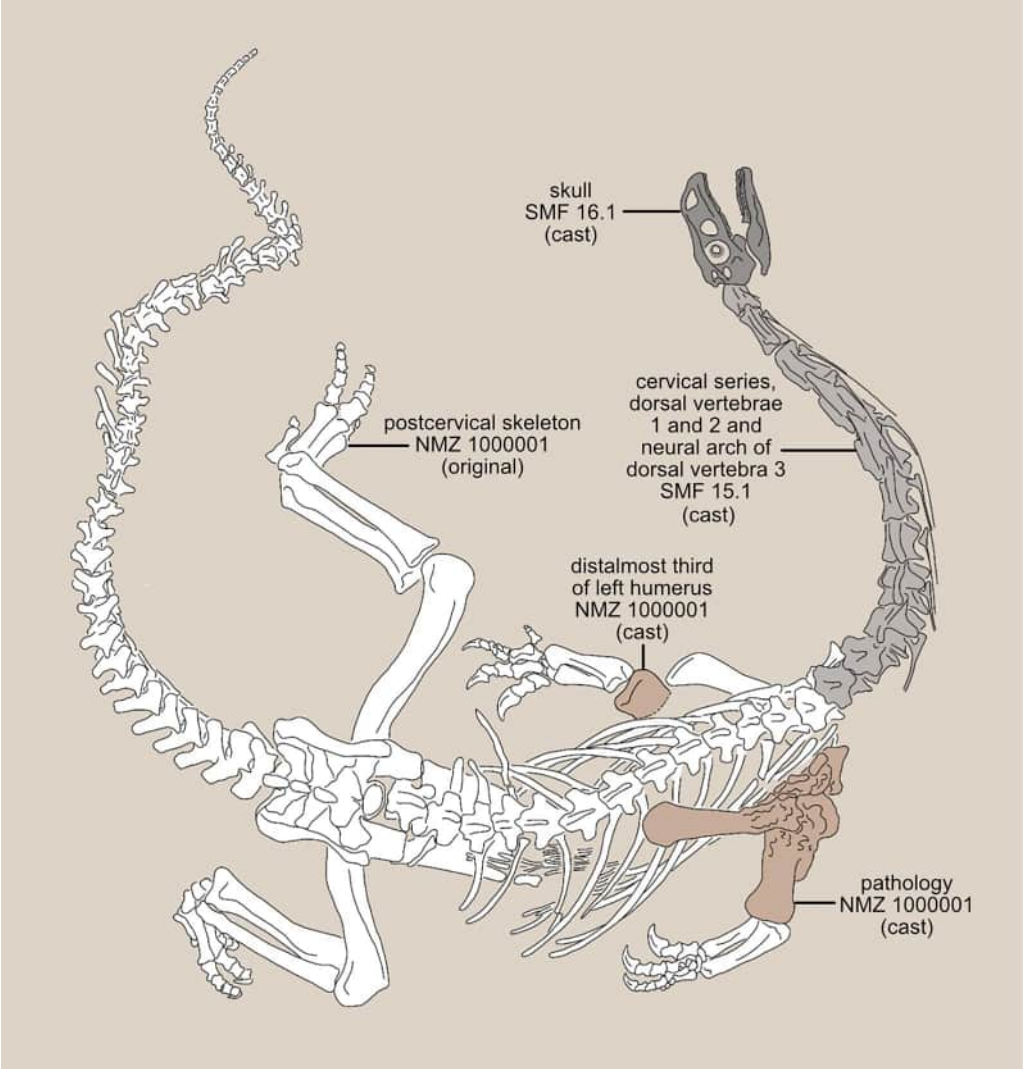

Fig. 2 Diagram of the *Plateosaurus trossingensis* skeleton as part of the Teoplati exhibit at the Natural History Museum of the University of Zurich. Diagram colour-coded by specimen (excavation ID used for all specimens for consistency) and material type that comprises the display skeleton

Investigation of the scapula-humerus pathology of NMZ 1000001 included comparisons with a currently undescribed *P. trossingensis* specimen from the Middle Saurian Level of the Gruhalde Quarry in Frick (SMF 11.4) which also exhibits a skeletal pathology. The specimen comprises a left and right radius and ulna with the left pair (specimen sub-numbers 11.4.144 and 11.4.189 respectively) exhibiting morphological deformation and likely pathological tissues along their midshafts. Such comparisons enable more robust assessments of pathology severity and aetiology.

For osteological study, measurements of up to 130 mm were taken using an analogue vernier calliper to the nearest millimetre and measurements greater than 130 mm were taken using a measuring tape to the nearest millimetre. Photographs of NMZ 1000001 were taken with a Canon 90D and a Sigma 18–35 f/1.8 Art lens, and of SMF 11.4 with a Nikon D2X and an AF Nikkor 50–75 lens.

CT-scan data acquisition

To fully investigate pathology characteristics and severity, the right pectoral girdle and upper forelimb of NMZ 1000001, comprising the humerus, scapula, coracoid and possible clavicle, as well as the pathological and normal radii and ulnae of SMF 11.4, were all scanned using computed tomography (CT) facilities at EMPA (Dübendorf, Switzerland) to identify modifications to internal bone structures and the immune responses of affected bones. Some elements were scanned both

individually and in articulation with neighbouring elements to help assess degrees of pathology-related element fusion. Two scans that each contain several articulated elements, as preserved, were thus produced of NMZ 100001: i) the proximal half of the scapula, including the scapular head, and the acetabular portion of the coracoid; and ii) the humerus and antero-proximal margins of the scapula, including the scapula head. These scans were acquired using a Linear Accelerator (LINAC) system (US-Photon, Hayward, California) with a maximum photon energy of 6 MeV, average electron current of 110 µA, and 177 pulses per second. The detector is a fan-shaped array of 3712 pixels with a pixel width of 0.4 mm. The integration time per projection is six pulses (0.036 s exposure time per projection) and 3600 projections are acquired to reconstruct each slice. The sample was placed between detector and the source (source-object distance = source-detector distance = 1000 mm) resulting in magnification of 2, therefore the effective pixel size is 0.2 mm. The 'individual element' scans of NMZ 1000001 comprise: i) the distalmost third of the right humerus; and ii) the potential clavicle and the acetabular portion of the coracoid. The radii and ulnae of SMF 11.4 were all scanned together. These scans were acquired using a RayScan (Meersburg, Germany) micro-CT device, with a peak photon energy of 270 keV and a current of 250 µA. The projections were formed using a 2048 by 2048 pixels array with a physical pixel size of 200 µm. Given the source-object distance (= 849.96 mm), and source-detector distance (= 1407.57 mm), the effective voxel size of the scans is approximately 121 µm. The integration time for each projection was 2 s, and a total of 2070 projections were acquired on a full rotation.

The 3D CT datasets of the right pectoral girdle and upper forelimb are available on Morphosource [https://www.morphosource.org; project ID: 000715009].

Histological sectioning of material

To investigate the ontogenetic stage and possible life history of NMZ 1000001, four thin sections were acquired from the right-hand side of dorsal ribs number 7 and 10. The sampling area was determined based on the existing breaks between the individual blocks used for the transportation of the skeleton. As a result, the cut of dorsal rib 7 was made in the middle of the shaft, while dorsal rib 10 was cut more proximally, just beneath the dichocephalous head. The thin sections were prepared by Mr. Olaf Dülfer, preparator at the Bonner Institut für Organismische Biologie, Abteilung Paläontologie, University Bonn, Germany. All thin sections were examined using a Keyence VHX-7000 digital microscope. Images of the thin sections were made under normal and cross-polarised light, each at × 40 and × 80 magnification. The histological terminology used herein mainly follows Buffrénil and Quilhac (2021) and Buffrénil et al. (2021).

Results

Osteological description of NMZ 1000001

Vertebrae

Dorsal vertebrae—Since the dorsal column has only been prepared from the dorsal and, where possible, right sides, most of the preserved dorsal vertebrae are represented solely by neural arches and the partially exposed right lateral surfaces of the centra. If preserved, the centrum is generally deformed with the dorsal half posteriorly shifted. The height and length of the vertebrae changes throughout the series (Table 1). Dorsal vertebrae 3 and 4 exhibit shorter centrum lengths than most other dorsals (Table 1). Moving posteriorly, dorsal vertebra 10 exhibits the longest centrum length at 116 mm and dorsal vertebra 11 exhibits the tallest maximum vertebra height at 128 mm (Table 1). Between dorsals 11–15 in an anterior–posterior direction, the maximum vertebra height and centrum length decreases (Table 1).

The neural spine of dorsal vertebra 4 is the shortest of the preserved series, both dorsoventrally and anteroposteriorly, and is subrectangular in dorsal view (Fig. 3). The anterior margin of the neural spines of dorsal vertebrae 4–5 is bifurcated (Figs. 3 and 4). Posteriorly, the neural spines of dorsal vertebrae 5–7 progressively increase in both anteroposterior and mediolateral extents, becoming weakly teardrop-shaped in dorsal view, while in dorsal vertebrae 8–15 the neural spines increase in mediolateral width and are subrectangular (Fig. 4). Dorsal vertebra 10 has the longest neural spine with a total length of 114 mm. The mediolaterally narrowest neural spine is that of dorsal vertebrae 4 and 9 at 18 mm, and the widest is that of dorsal vertebra 15 at 41 mm. The posterior margin of the neural spines of dorsal vertebrae 13–15 is bifurcated (Fig. 5). Both the spinoprezygapophyseal and spinopostzygapophyseal fossae are somewhat prominent in dorsals 4–7 and are more strongly developed in dorsals 11–15 (Figs. 3, 4 and 5).

Prezygapophyses are rather poorly preserved and closely articulated in dorsal vertebrae 4–7 and, despite close articulation of the vertebrae, are mostly well preserved in dorsal vertebrae 8–10 (Figs. 4 and 5). They are dorsally exposed in dorsal vertebrae 11 and 15, while in dorsal vertebrae 12–14 they are mostly hidden from view. The prezygapophyses of dorsal vertebra 4 are short and wide but become more elongate in dorsal vertebrae 5 and 6 (Figs. 3 and 4). In dorsal vertebrae 7–11 the prezygapophyses decrease in both length and diameter (Table 1). The prezygapophyses articular facets of dorsal

Table 1 Dorsal vertebral measurement series of *Plateosaurus trossingensis* NMZ 1000001

Vertebra	zgl	vh	cl	ch	tw	nsl	nsh	nsw
do3	–	–	104	–	–	–	–	–
do4	127	125	> 100	> 40	144	40	15	18
do5	> 118	> 56	–	–	145	76	20	20
do6	~ 126	> 46	–	–	158	80	22	20
do7	~ 133	> 43	–	–	155	92	26	21
do8	> 135	> 53	–	–	154	104	25	19
do9	> 150	> 54	–	–	152	106	26	18
do10	~ 170	~ 106	116	–	171	114	29	22
do11	150	128	110	~ 68	182	105	33	24
do12	> 135	115	> 107	–	191	84	~ 37	23
do13	145	115	109	> 62	181	73	~ 36	25
do14	143	~ 100	108	> 58	173	66	~ 44	30
do15	139	~ 92	100	> 34	~ 170	54	~ 57	41

Note that dorsal vertebrae 1 and 2 and the neural arch of dorsal vertebra 3 were not preserved and thus measurements are not given. *ch* centrum anterior height, *cl* centrum length, *do* dorsal vertebra, *nsh* neural spine height, *nsl* neural spine length, *nsw* neural spine maximum width, *tw* transverse width across the diapophyses, *vh* maximum vertebra height, *zgl* zygapophyseal length. All measurements in mm

vertebra 11 are elliptical, while in dorsal vertebrae 15 they are more subcircular (Fig. 5).

The diapophyses of dorsal vertebrae 4–10 are horizontal and posterolaterally orientated (Figs. 3 and 4). In dorsal vertebrae 11–15, they become more laterally-orientated. Anteriorly, the diapophyses are wing-like processes bearing large articular facets, which have ovoid shapes in dorsal vertebra 4, while in the succeeding dorsals they become progressively flatter with lenticular, concave articular facets (Figs. 3 and 4). In dorsal vertebrae 13 and 15, the diapophyses are co-ossified to dorsal ribs 13 and 15. Where exposed, both the anterior and posterior surfaces of the centrum are concave in all dorsals (Fig. 5). The centra of dorsal vertebrae 4–10 are mostly buried in sediment and are only partially visible in posterior dorsals 11–15. The exposed portions of the centra are shorter in the anterior dorsals but become slightly more elongated in the mid-dorsal series before decreasing again in length in the last dorsals. In dorsal vertebrae 11–14, a fossa in the right lateral side of the centrum is visible, amplifying the bulging lip-like appearance of the anterior and posterior margins of the articular surfaces (Fig. 5).

Parapophyses are well exposed in dorsal vertebra 4 (Fig. 3) but are not as well preserved in the succeeding dorsals (Figs. 4 and 5). In the more posterior dorsals, the parapophyseal facet becomes smaller and more elongate compared to those of dorsals 4–6 (Figs. 3, 4 and 5).

Dorsal ribs—NMZ 1000001 has 28 dorsal ribs, with 14 elements corresponding to the left and 14 to the right side. Apart from varying degrees of post-mortem or post-depositional fractures, the shafts are generally well-preserved, while the costal heads are mostly either poorly preserved, covered by bones or buried in matrix. The recorded measurements pertain to the exposed portions of the rib shafts only. The right dorsal rib 13 is proximally fused to the corresponding dorsal vertebra 13 and is generally well preserved in one piece (Fig. 6).

The anterior dorsal ribs are the longest and most robust of the dorsal ribs and become shorter and less robust as the series moves posteriorly. Passing posteriorly, the tuberculae progressively decrease in size while the capitulae become more prominent. The parapophysis gradually migrates from a position dorsal to the centrum to anterior to the diapophysis, a corresponding shift of the costal articular facets of the dorsal ribs should be apparent. However, this is not clearly discernible as anatomical details of the proximal head are mostly only partially exposed or obscured by poor preservation. In dorsal rib 14, both articular processes of the costal head are smaller than in the anterior or mid-dorsal ribs.

The proximodistal length of the rib shafts ranged up to 80 cm in the right dorsal rib 5. The anterior and mid-dorsal ribs are slightly ventromedially curved, while posterior ribs are mostly straight. In dorsal ribs 3–9, a prominent rim extends distally from the costal head along about two-thirds of the upper posterior surface of the shaft. The proximal half of each shaft has a pretty much constant diameter. Distally, the shaft tapers slightly. The distal ends of the mid-dorsal ribs are rounded, while in the posterior ribs the anterior corner is more pointed (Fig. 6).

Sacrum—The sacrum comprises two primordial sacral vertebrae followed by one caudosacral vertebra.

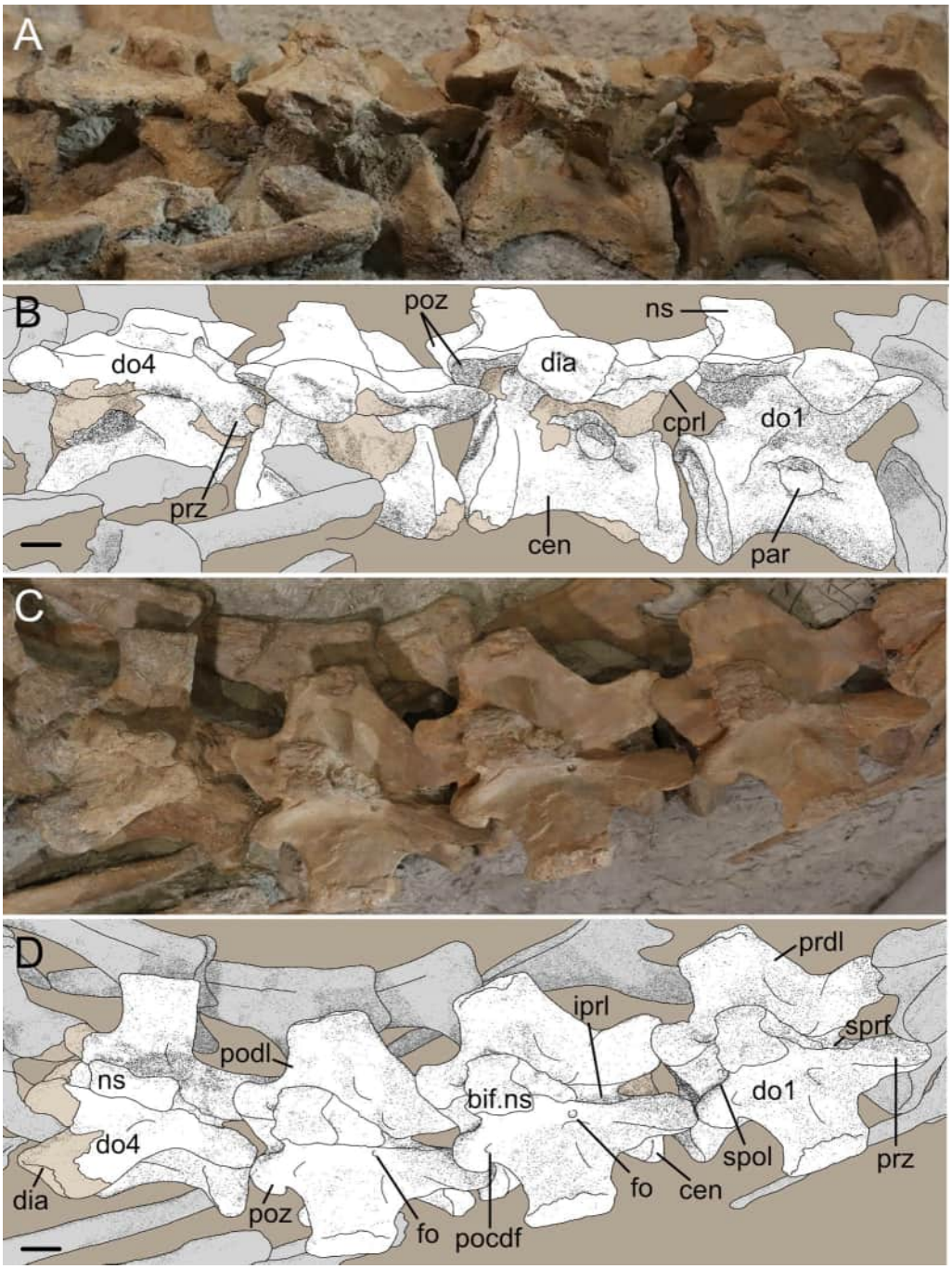

Fig. 3 Anterior dorsal vertebrae of *Plateosaurus trossingensis* NMZ 1000001. **A** photograph and **B** interpretive drawing of the first to fourth dorsal vertebrae in right lateral view. **C** photograph and **D** interpretive drawing of the vertebrae in dorsal view. Note that dorsal vertebrae 1 and 2 and the neural arch of dorsal vertebra 3 were not preserved and are represented here by SMF 15.1. *bif* bifurcated, *cen* vertebral centrum, *cprl* centroprezygapophyseal lamina, *dia* diapophysis, *do* dorsal vertebra, *fo* foramen, *iprl* intraprezygapophyseal lamina, *ns* neural spine, *par* parapophysis,, *pocdf* postzygapophyseal centrodiapophyseal fossa, *podl* postzygadiapophyseal lamina, *poz* postzygapophysis, *prdl* prezygodiapophyseal lamina, *prz* prezygapophysis, *spol* spinopostzygapophyseal lamina, *sprf* spinoprezygapophyseal fossa. Scale bars 20 mm

The sacrum is preserved in full articulation with the ilia in semi-articulation with caudal vertebra 1 and is disarticulated from the posteriormost element of dorsal vertebra 15 (Fig. 15). The sacrum is dorsally exposed with the centra ventrally stuck within the matrix. The only visible part of the centrum of sacral vertebra 1

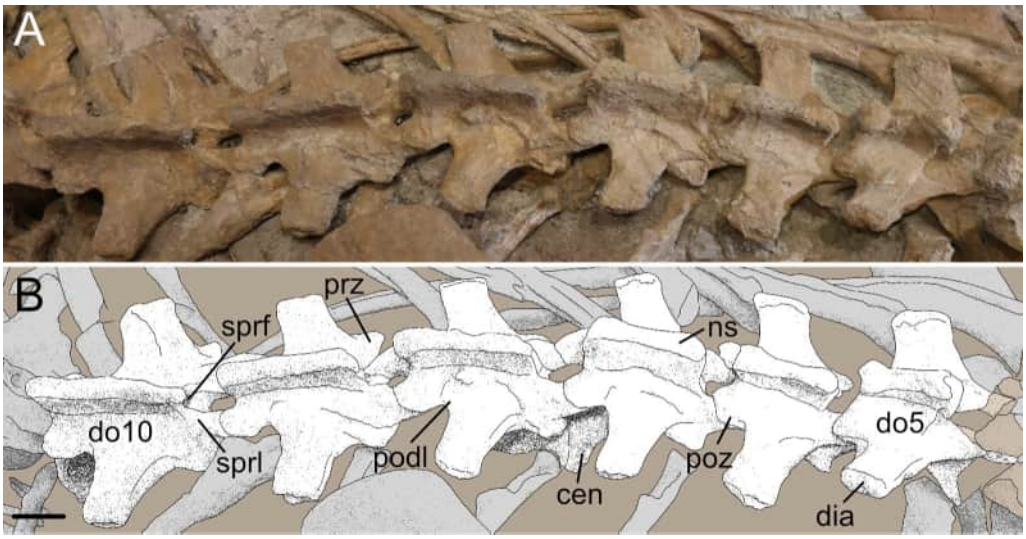

Fig. 4 Middle dorsal vertebrae of *Plateosaurus trossingensis* NMZ 1000001. **A** photograph and **B** interpretive drawing of the fifth to tenth dorsal vertebrae in right laterodorsal view. *cen* vertebral centrum, *dia* diapophysis, *do* dorsal vertebra, *ns* neural spine, *podl* postzygadiapophyseal lamina, *poz* postzygapophysis, *prz* prezygapophysis, *sprf* spinoprezygapophyseal fossa, *sprl* spinoprezygapophyseal lamina. Scale bars 40 mm

is its anterior portion. Apart from minor degrees of dorsoventral compression, the sacrum is well preserved. The maximum anteroposterior length of the sacrum, including the space between the sacrals, is 38 cm (Table 2).

The neural arches of all three sacral vertebrae have a dorsoventrally flattened shape and are anteroposteriorly elongated and mediolaterally wide (Table 2). The neural spine of sacral vertebra 1 is subrectangular in dorsal view, with an anteroposterior length approximately two times its mediolateral width. For sacral vertebrae 2 and 3, the neural spine has a slightly teardrop-shaped appearance with a posterior end that is expanded mediolaterally (Fig. 7). In contrast to the posterior dorsals, the neural spines of the sacrals do not possess a bifurcated posterior margin. In lateral view, the dorsal margin of all three neural spines is subhorizontal and straight.

Close articulations of the sacral vertebrae cover the majority of both the anterior and posterior zygapophyses in the sacrum, leaving only the articular surfaces of the prezygapophyses of sacral vertebra 1 and the postzygapophyses of sacral vertebra 3 exposed (Fig. 7). In sacral vertebra 1, the prezygapophyses bear large dorsomedially orientated rounded facets with straight dorsal margins, while the postzygapophyses are noticeably smaller. The same is true for both articular surfaces of sacral vertebrae 2 and 3, where the zygapophyses are only about 60% the size of the prezygapophyses in sacral vertebra 1. The postzygapophyses of sacral vertebra 3 feature ventrolaterally orientated articular facets with slightly concave ventral margins.

The centrum of sacral vertebra 1 is tilted posteriorly, causing its anterior surface to be orientated slightly towards the anterodorsal direction in relation to the rest of the sacrum. The articular surface is elliptical in anterior view and is 88 mm high and 135 mm wide. The anterior surface is slightly concave with well-defined low margins (Fig. 7).

All three pairs of sacral ribs are preserved, proximally fused to the sacral vertebrae and distally in close contact to the medial surface of the iliac blade. The division between the costal head and the articulation processes of the sacral vertebrae is not clearly visible. The sacral ribs are mostly complete, except for the posterior margin of the left rib in sacral vertebra 1 and the right rib in sacral vertebra 3, which are both missing.

Sacral rib 1 expands in an anterolateral direction, while sacral ribs 2 and 3 are more posterolaterally orientated. In dorsal view, the maximum proximodistal extents of sacral ribs 1–3 are around 162 mm, 145 mm and 134 mm respectively. The sacral ribs are somewhat mushroom-shaped with an anteroposteriorly enlarged proximal head, a constricted midshaft and a greatly expanded distal end. In dorsal view, the anteroposterior length of the contact surface at the iliac blade for sacral ribs 1–3 are 42 mm, 66 mm and 84 mm, respectively. The anterior surface appears rather convex in sacral ribs 1 and 2 but is concave in sacral rib 3. In sacral rib 1, the anteroventral portion of the shaft forms a large, anteriorly extending flange with a convex margin (Fig. 7).

Caudal vertebrae—The caudal series is represented by 48 generally articulated vertebrae, apart from some

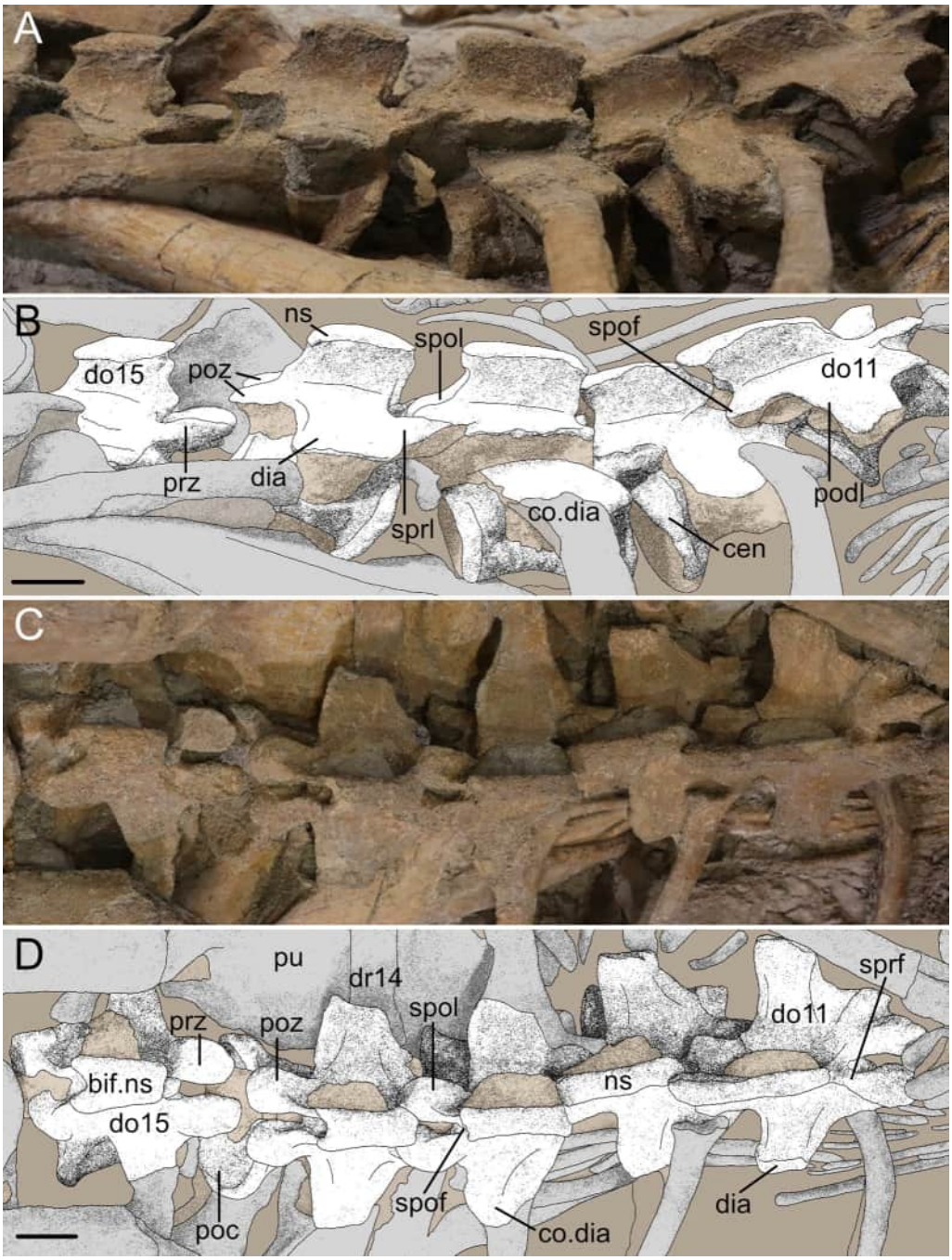

Fig. 5 Posterior dorsal vertebrae of *Plateosaurus trossingensis* NMZ 1000001. **A** photograph and **B** interpretive drawing of the eleventh to fifteenth dorsal vertebrae in right lateral view. **C** photograph and **D** interpretive drawing of the vertebrae in dorsal view. *bif* bifurcated, *cen* vertebral centrum, *co* co-ossified, *dia* diapophysis, *do* dorsal vertebra, *dr* dorsal rib, *ns* neural spine, *poc* posterior centrum surface, *podl* postzygadiapophyseal lamina, *poz* postzygapophysis, *prz* prezygapophysis, *pu* pubis, *spof* spinopostzygapophyseal fossa; *spol* spinopostzygapophyseal lamina, *sprf* spinoprezygapophyseal fossa, *sprl* spinoprezygapophyseal lamina. Scale bars 30 mm

post-depositional fractures, spanning a preserved length of 332 cm along the vertebral axis (series not complete as the distal end is missing). The orientation and completeness of individual elements varies throughout the caudal series. Caudal vertebrae 1–9 are laying on their right side with the left lateral surfaces of the neural spines, neural arches and centra all exposed, and the dorsal and ventral surfaces of the left transverse processes

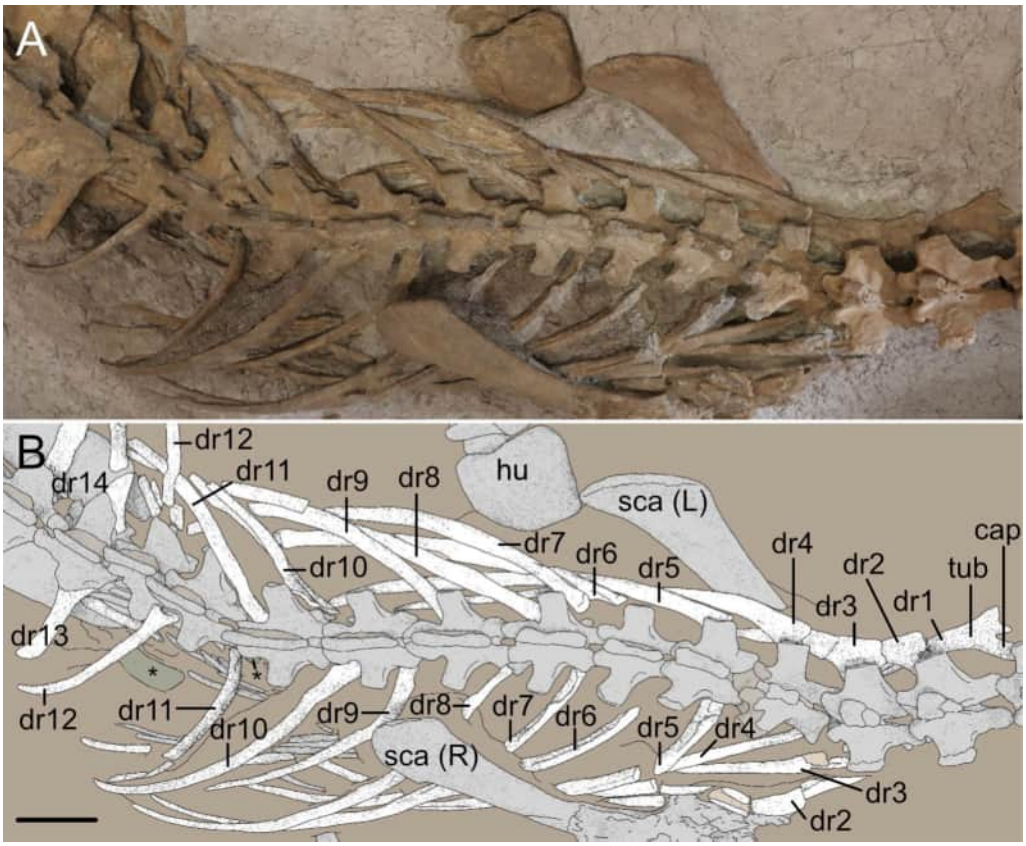

Fig. 6 Dorsal ribs of *Plateosaurus trossingensis* NMZ 1000001. **A** photograph and **B** interpretive drawing of the first to fourteenth dorsal ribs in dorsal view. *cap* capitulum, *dr* dorsal rib, *hu* humerus, *L* left, *R* right, *sca* scapula, *tub* tuberculum. Bone marked with asterisks denote unidentified bone fragments in the abdominal region that likely do not belong to NMZ 1000001. Scale bars 10 cm

exposed (Fig. 8A–D). In addition, the corresponding haemal arches are mostly articulated and situated ventrally to the vertebrae. The vertebrae posterior to caudal vertebrae 9 are orientated in a more upright position in caudal vertebrae 10–14, and in an entirely upright position in caudal vertebrae 15 and 16, with both left and right transverse processes visible and their left ventral halves including the haemal arches struck in the sediment (Fig. 8C–F). Moving posteriorly, the tail bends to one side, exposing the right lateral surface of caudal vertebrae 17–29, before abruptly flipping over so that caudal vertebrae 30–47 are situated with their left side up (Figs. 8E, F, 9). The orientation of caudal vertebra 48 is difficult to determine due to being only partly and poorly preserved (Fig. 9C, D). In caudal vertebrae 37–44 the neural suture is faintly visible.

Table 2 Sacral measurements of *Plateosaurus trossingensis* NMZ 1000001

Vertebra	zgl	ch	nsl	nsh	nsw
sa1	118	88	69	33	39
sa2	> 104	–	79	33	42
sa3	~ 121	–	96	33	49

ch centrum anterior height, *nsh* neural spine height, *nsl* neural spine length, *nsw* neural spine maximum width, *sa* sacral vertebra, *zgl* zygapophyseal length. All measurements in mm

The caudal series can be loosely divided into three major regions based on their morphological differences: anterior caudals (1–6); middle caudals (7–26); and posterior caudals (27–48; Figs. 8 and 9). The centra of the anterior caudals exhibit greater heights and widths than lengths (Table 3). Along the middle and posterior elements, the vertebrae become proportionally longer and narrower, especially towards the distal end of the tail.

In all caudal vertebrae, the neural spines are posteriorly orientated (Figs. 8 and 9). The neural spines of the anterior caudals are dorsoventrally tall, making up around 35% of the total dorsoventral height of caudal vertebrae 1–4, and 43% in caudal vertebrae 5 and 6. In lateral view, the dorsal margin is mostly subhorizontal to slightly convex. In the middle caudals, the neural spine progressively decreases in both height and length

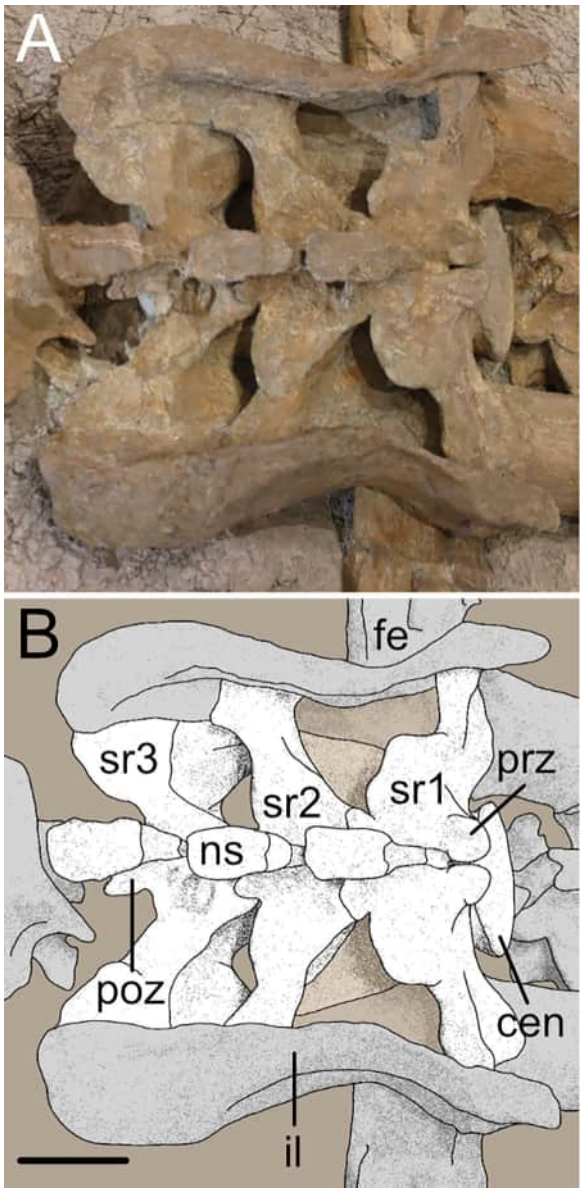

Fig. 7 Sacrum of *Plateosaurus trossingensis* NMZ 1000001. **A** photograph and **B** interpretative drawing of the first to third sacral vertebrae in dorsal view. *cen* vertebral centrum, *fe* femur, *il* ilium, *ns* neural spine, *poz* postzygapophysis, *prz* prezygapophysis, *sr* sacral rib. Scale bar 10 cm

while simultaneously becoming more angular and sloped posteriorly with a convex dorsal margin (Fig. 9A, B). In the posterior caudals, the neural spine migrates further posteriorly and reduces in height. In caudal vertebra 36, the neural spine is reduced to a knob-like process located between the postzygapophyses (Fig. 9C, D).

The posterior caudal prezygapophyses are larger relative to those of anterior and middle caudals and surpass the anterior margin of the centrum by approximately 10% of the total vertebrae length. The articulation facets are generally weakly convex and in the anterior caudals are mediodorsally orientated at approximately 45 degrees with respect to the horizontal plane. In the middle caudals (11–16), the articulation facets angles are approximately 55 degrees with respect to the horizontal plane.

Similar to the prezygapophyses, the postzygapopohyses of the anterior and anterior-middle (7–10) caudals are small relative to the overall size of the vertebrae, and are larger, relative to vertebrae size, in the rest of the middle caudals and posterior caudals. However, in contrast to the prezygapophyses, which emerge right above the neurocentral suture, the position of the postzygapohyses is dorsal to the base of the neural spine. As a result of the posteriorly-sloped spine, postzygapophyses overhang the centra to a greater degree (around 15–22%). In the posteriormost caudals (40–47) both the pre- and postzygapophyses become indiscernible.

From caudal vertebrae 1–5, the centra exhibit a greater dorsoventral height than anteroposterior length (Table 3). Moving posteriorly, the relative centrum length progressively increases so that starting from caudal vertebra 8, the centra are longer than tall (Table 3). The midsection is generally slightly constricted and exposed anterior and posterior surfaces are amphicoelous. A shallow groove on the ventral surface of the centrum is present in caudal vertebrae 1–6 and 17–21.

The caudal transverse processes are flat, posterolaterally orientated plates that progressively decrease in both size and robustness through the caudal series and in anterior–posterior direction and disappear entirely posterior to caudal vertebra 28 (Figs. 8 and 9). In the anteriormost seven caudals, the distal end of the processes expands anteroposteriorly, resulting in a spatulate-like appearance with a convex lateral margin in dorsal view, whereas from caudal vertebra 8 the distal end is of subequal width as the proximal end. Passing distally from caudal vertebra 15, the transverse processes are distally tapering with a rounded distal margin.

A total of 41 Y-shaped haemal arches are preserved, most of them in semi-articulation and, at least partially, obscured by overlaying elements or matrix. Several haemal arches are affected by fractures or deformations, most likely resulting from post-depositional pressure. Haemal arch 17 exhibits an unusually formed distal end of the shaft (as originally described by Schaeffer et al., (2024); Fig. 8E and F). Where exposed, the articular facets appear oval or saddle-shaped. Haemal arches 1–4 appear smaller than the succeeding arches 5–9 (Fig. 8A–D). Haemal arches 9 and 10, which have proximodistal lengths of 227 mm and 193 mm, respectively, are almost completely exposed (Fig. 8C and D; Table 3). In haemal

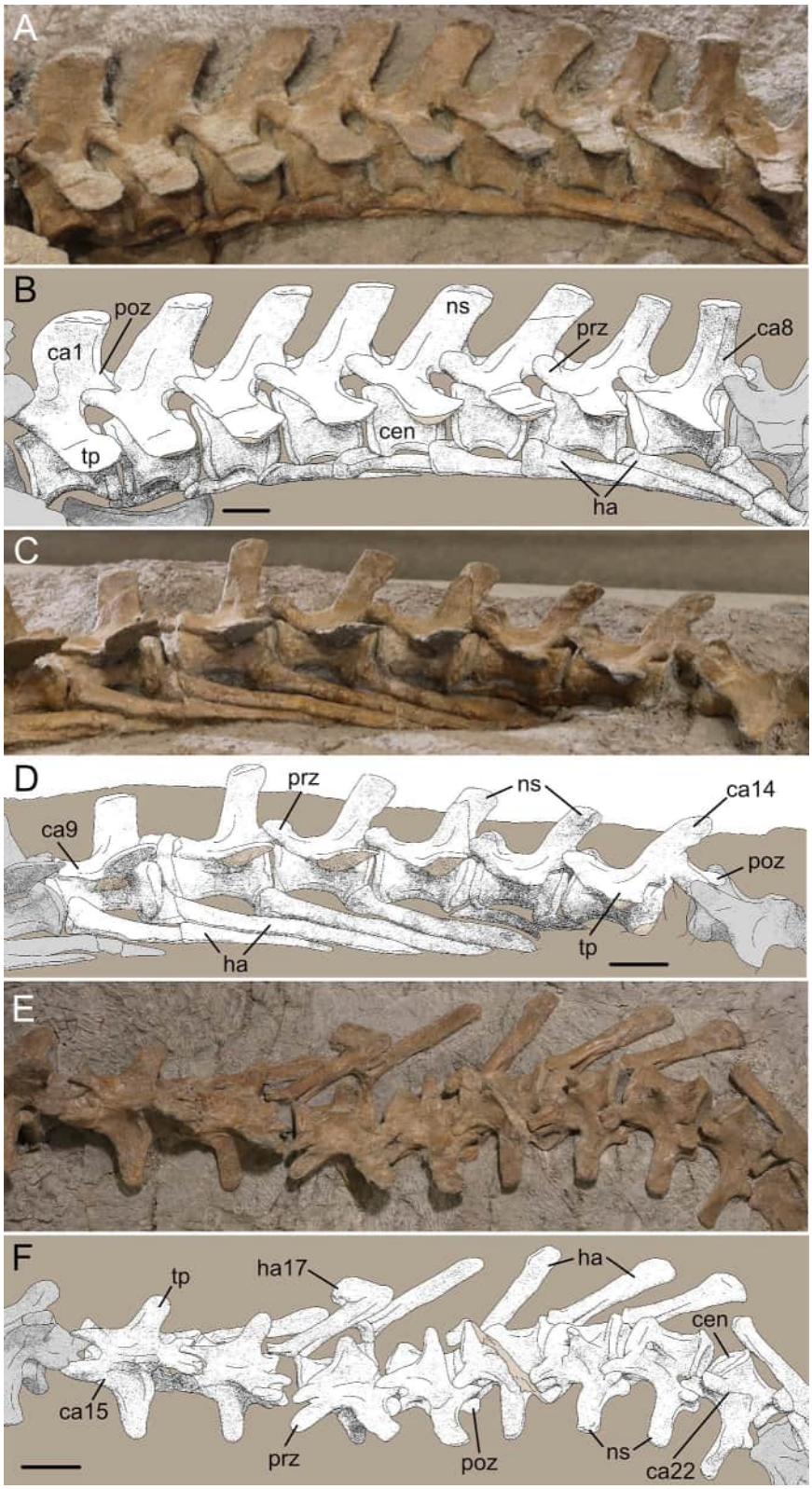

Fig. 8 Anterior and middle caudal vertebrae of *Plateosaurus trossingensis* NMZ 1000001. **A** photograph and **B** interpretive drawing of the first to eight caudal vertebrae in left lateral view. **C** photograph and **D** interpretive drawing of the ninth to fourteenth caudal vertebrae in left lateral view. **E** photograph and **F** interpretive drawing of the fifteenth to twenty-second caudal vertebrae in right dorsolateral view. *ca* caudal vertebrae, *cen* centrum, *ha* haemal arch, *ns* neural arch, *poz* postzygapophysis, *prz* prezygapophysis, *tp* transverse process. Scale bar 50 mm

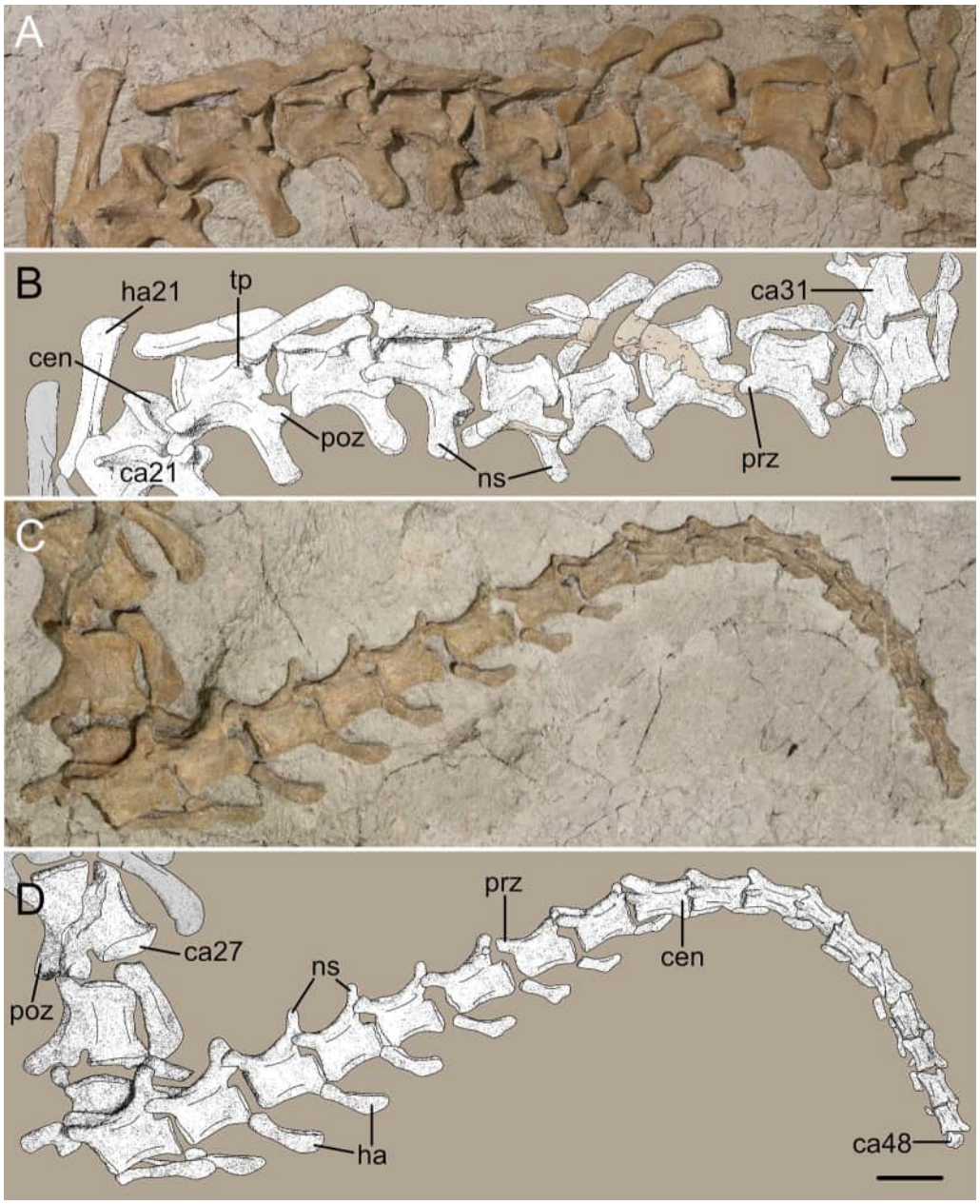

Fig. 9 Middle-posterior and posterior caudal vertebrae of *Plateosaurus trossingensis* NMZ 1000001. **A** photograph and **B** interpretive drawing of the twenty-first to thirty-first caudal vertebrae in right lateral view. **C** photograph and **D** interpretive drawing of the twenty-seventh to forty-eighth caudal vertebrae in left lateral view. *ca* caudal vertebrae, *cen* centrum, *ha* haemal arch, *ns* neural arch, *poz* postzygapophysis, *prz* prezygapophysis, *tp* transverse process. Scale bar 50 mm

arch 19, the enclosed opening of the teardrop shaped haemal canal occupies approximately 13% of the total length of the haemal arch. The shafts are mostly straight or slightly posteroventrally convex, and mediolaterally flattened. The distal ends of the haemal arches are anteroposteriorly expanded to a distinct spatulate shape with convex (15–32) or straight (33–45) ventral margin (Figs. 8E, F and 9). Due to poor preservation the haemal arches posterior to haemal arch 45 are largely indiscernible.

Gastralia

The gastral apparatus is represented by a slab of 41 rod-like bony fragments, comprising 31 individual gastral

Table 3 Caudal vertebral measurement series of *Plateosaurus trossingensis* NMZ 1000001

Vertebra	zgl	vh	cl	ch	tw	nsl	nsh	nsw
ca1	~121	207	81	82	108	60	68	~24
ca2	125	198	80	82	100	50	76	25
ca3	128	210	78	83	97	46	71	24
ca4	128	208	77	79	98	48	75	>15
ca5	~130	195	78	78	91	56	83	>16
ca6	~126	194	79	75	88	44	87	>11
ca7	125	184	75	~71	86	36	73	13
ca8	~125	158	80	>60	83	40	65	14
ca9	119	153	79	>56	79	38	61	~12
ca10	116	150	80	>55	68	34	59	12
ca11	~112	140	79	>45	66	33	55	13
ca12	115	129	82	>42	61	35	46	14
ca13	112	118	78	>40	56	28	37	16
ca14	~115	>109	81	>38	53	27	34	12
ca15	~110	>70	~80	>20	50	30	31	12
ca16	104	>76	78	>33	41	28	29	13
ca17	~100	>100	75	>41	36	24	28	>8
ca18	96	>100	~66	42	32	26	28	~11
ca19	~91	109	64	42	26	21	30	8
ca20	>80	110	>62	>38	23	20	~34	~8
ca21	85	111	63	~44	20	20	35	>5
ca22	84	>98	62	43	18	19	36	>2
ca23	>72	~102	67	~40	16	22	38	>3
ca24	77	~94	61	>27	13	22	31	>4
ca25	74	~92	57	40	7	15	28	~2
ca26	73	84	56	~36	6	15	19	2
ca27	71	80	55	35	–	14	>13	2
ca28	~68	77	55	33	0	13	19	2
ca29	>57	>52	>46	32	0	12	17	2
ca30	67	68	49	26	0	10	13	2
ca31	62	63	46	25	0	9	11	~2
ca32	~58	59	44	25	0	7	9	~1
ca33	55	56	43	22	0	6	8	~1
ca34	~55	53	41	>16	0	6	8	1
ca35	~52	47	46	18	0	6	6	1
ca36	~48	42	38	19	0	4	5	1
ca37	46	36	37	16	0	4	3	1
ca38	44	31	36	12	0	0	0	~1
ca39	43	29	34	~10	0	0	0	0
ca40	42	24	33	~9	0	0	0	0
ca41	~40	22	31	~9	0	0	0	0
ca42	~40	23	30	~8	0	0	0	0
ca43	~38	21	29	~8	0	0	0	0
ca44	~36	19	25	~8	0	0	0	0
ca45	~33	19	23	~9	0	0	0	0
ca46	~29	18	~21	~8	0	0	0	0
ca47	~25	~17	~20	~7	0	0	0	0
ca48	~10	~14	~13	-	0	0	0	0

ca caudal vertebra, *ch* centrum anterior height, *cl* centrum length, *nsh* neural spine height, *nsl* neural spine length, *nsw* neural spine maximum width, *tw* transverse width across the diapophyses, *vh* maximum vertebra height, *zgl* zygopophyseal length. All measurements in mm

elements, most of which are at least partially covered by matrix and/or dorsal ribs. As most of these pieces are fragmented and poorly preserved, it is not possible to confidently identify individual bones. Based on their size and location within NMZ 1000001, these elements can be roughly separated into two groups; a smaller, gracile group situated medially and slightly posteriorly to the larger, more robust group (Fig. 10). Approximately 22 of the smaller pieces are interpreted as medial gastralia and 12 larger of the larger pieces as lateral gastralia (Fig. 10). The maximum diameter of the medial elements range between 3 and 10 mm, while the lateral element diameters range between 5 and 12 mm. The longest preserved medial gastralia measures approximately 193 mm, while the longest lateral gastralia measures 135 mm.

Pectoral girdle

The left pectoral girdle is only represented by a partial scapula while the right is fairly complete and comprises the scapula, coracoid and possible remnants of the clavicle. Based on the completeness of NMZ 1000001, the coracoid and clavicle of the left side might have been preserved, but are likely still covered in sediment.

Scapulae—The scapulae are long and flat and the shafts are slender and increase in width towards the posterior end. Only the scapular blades and the distal portions of the shafts are exposed and well-preserved, as the left scapula is partially obscured by matrix and overlying bones, while the proximal half of the right scapula is deformed with the scapula head completely separated from the shaft by proliferated bone growth (Fig. 11).

The left scapula is partially covered by matrix and the superimposed dorsal vertebra 4 and dorsal ribs 3 and 4, with the proximal third of the scapula being medially exposed. The visible part of the scapula has a proximodistal length of 325 mm. The shaft is smallest dorsoventrally, measuring 85 mm wide, and is situated about 270 mm proximal to the distal margin of the scapular blade. Distally, the height of the shaft exhibits a maximum height of 172 mm just 30 mm from the distal margin.

The right scapula has the lateral surface dorsally exposed and is situated on the right side of the spinal column at the level of dorsal vertebrae 4–9, overlaying dorsal ribs 3–8. The unaffected (=normal) portion of the scapula measures around 310 mm, which comprises 70% of the estimated total length of the bone. The convex distal margin of the scapular blade bears a small flange at the proximoventral corner. At 175 mm, the maximum dorsoventral extent of the distal end is two times that of the minimum shaft length, which is just distal to the anteriormost part of the normal shaft (Fig. 11).

The scapular head, disconnected from the rest of the scapula by proliferated bone growth, is situated approximately 170 mm anterior to the shaft (Fig. 11). The head has a dorsoventral length of 132 mm and a maximum proximodistal length of 66 mm. With an

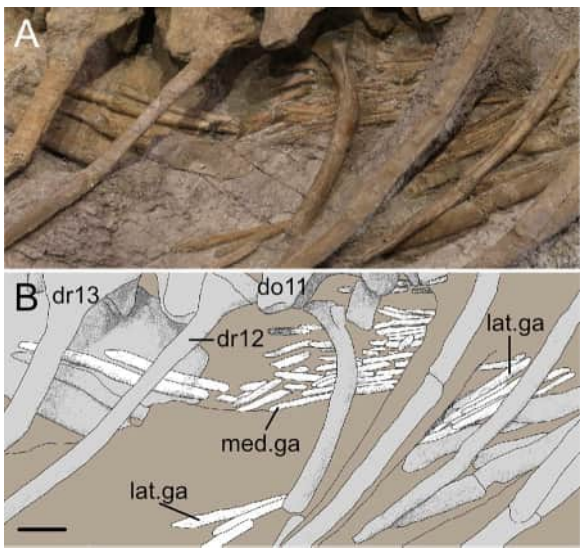

Fig. 10 Gastral apparatus of *Plateosaurus trossingensis* NMZ 1000001. **A** photograph and **B** interpretive drawing of several medial and lateral gastralia in right dorsolateral view. *do* dorsal vertebra, *dr* dorsal rib, *ga* gastralia, *lat* lateral, *med* medial. Scale bars 30 mm

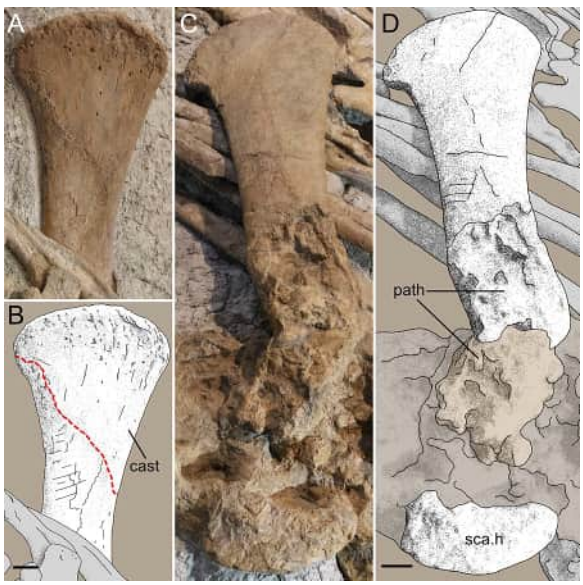

Fig. 11 Scapulae of *Plateosaurus trossingensis* NMZ 1000001. **A** photograph and **B** interpretive drawing of the left scapula in medial view, with cast replica material highlighted by the red dashed line. **C** photograph and **D** interpretive drawing of the right scapula in lateral view. *path* pathological tissue, *sca.h* scapula head. Scale bars 30 mm

approximate lateromedial width of 26 mm, it is thinner transversely than the distal end of the scapular blade. The proximal margin appears convex but is poorly preserved with a rough surface, along with a strongly deformed lateral surface, which prevents reliable identification of anatomical details.

Coracoid—Only the right coracoid is preserved, disarticulated from the scapula and situated adjacent to dorsal vertebrae 3 and 4. The anterior surface is visible laterally, while the posterior surface is obscured by matrix. The exposed surface and margins of the coracoid, especially the acetabular portion, is highly deformed. In ventral view, the visible portion of the coracoid is subrectangular, measuring 230 mm by 143 mm. The lateral surface is mostly flat and exhibits faint, anteroposteriorly directed striations, especially in its ventral half (Fig. 12A and B). The coracoid foramen is well-preserved with a diameter of around 14 mm and is located 74 mm dorsal to the convex lateral margin and 56 mm posteriorly to the slightly sigmoidal anterior margin. The anterior portion of the glenoid facet is subovoid-shaped.

Clavicle—Two small rod-like pieces of bone located on top of the deformed cluster which forms the right pectoral girdle might be possible remnants of the right clavicle (Fig. 12C and D). These pieces are 80 mm and 75 mm long, each with a maximum diameter of around 32 mm. The cross-sections of both elements are suboval. Based on their size, the two elements could also be interpreted as partial costal heads of a dorsal rib, such as the left dorsal rib 1, although confident identification of the two elements is impeded by their incompleteness and indistinctive morphology.

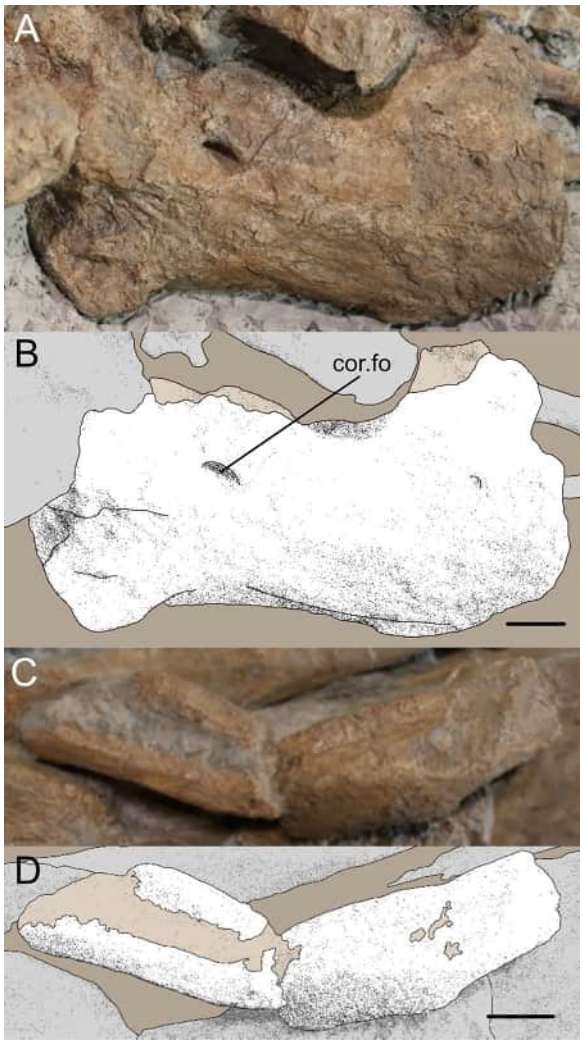

Fig. 12 Right coracoid and potential clavicle of *Plateosaurus trossingensis* NMZ 1000001. **A** photograph and **B** interpretive drawing of the right coracoid in anterior view. **C** photograph and **D** interpretive drawing of the potential right clavicle in anterior view. *cor.fo* coracoid foramen. Scale bars 30 mm (**A**, **B**) and 20 mm (**C**, **D**)

Forelimb

The left and right forelimbs are both almost completely preserved and are fully articulated.

Humeri—The right humerus and the distalmost third of the left humerus are described here as how they are preserved in the 'Teoplati' exhibit (Fig. 2). The description of the proximal two thirds of the left humerus can be found in the supplementary information.

The distal ends of both humeri are preserved in articulation with the radius and ulna. The left humerus is mostly exposed on the posterior and distal surfaces with only the distalmost 153 mm of the posterior surface and posterior half of the distal articular facet visible (Fig. 13A and B). The distal margin has a flat appearance. The visible part of the element has a maximum mediolateral length of 167.4 mm and exhibits a lightly sinus-shaped margin formed by a large, strongly convex ulnar condyle and a smaller, less-prominent radial condyle. The posterolateral surface at the base of the ulnar condyle is rugose and corresponds to the attachment site of the antebrachial muscles.

In the right humerus, the posterior surface as well as the posterior portions of the medial, lateral and distal surfaces are exposed. The preserved length of the humerus is 343 mm, but the overall bone length cannot be measured, nor can the morphology of the humeral head or deltopectoral crest be observed due to the heavily deformed proximal half of the bone (Figs. 13C, D, S1C and D; Table S1). In contrast to the scapula, where the boundary between the pathological and normal tissue is clear and distinct, the transition from pathological to normal tissue in the humerus is

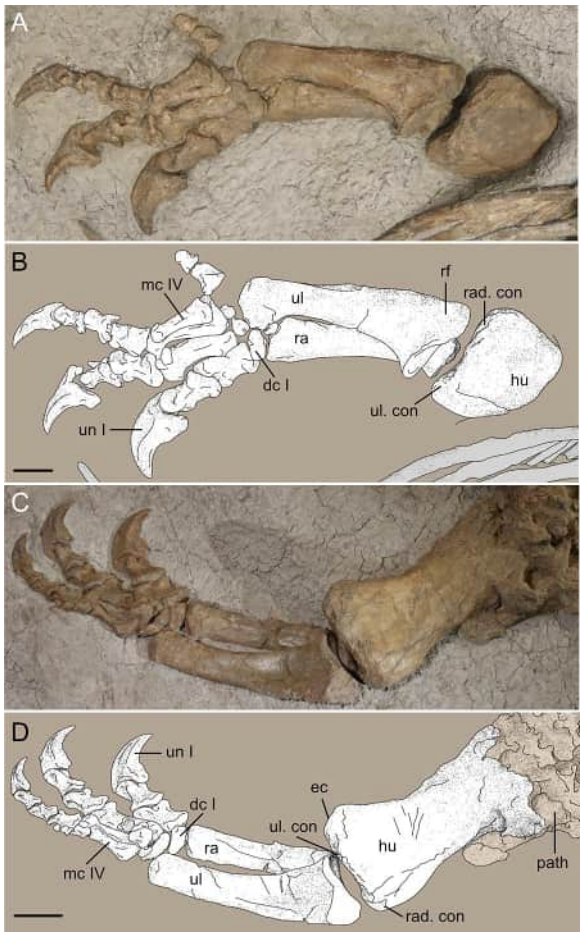

Fig. 13 Forelimbs of *Plateosaurus trossingensis* NMZ 1000001. **A** photograph and **B** interpretive drawing of the left forelimb in dorsal view. **C** photograph and **D** interpretive drawing of the right forelimb in dorsal view. *dc* distal carpal, *ec* entepicondyle, *hu* humerus, *mc* metacarpal, *path* pathological tissue, *ra* radius, *rad.con* radial condyle, *rf* radius face, *ul* ulna, *un* ungual. Scale bars 50 mm (**A**, **B**) and 70 mm (**C**, **D**)

more gradual (Figs. 11, 13, S1C and D). The preserved shaft is broadly elongate elliptical in cross section and is anteroposteriorly and mediolaterally wider than the shaft of the left humerus (Table S1). The distal end is slightly flattened and has a maximum mediolateral width of 174 mm. The width gradually decreases towards the midshaft until it reaches a minimum width of 110.2 mm around 134 mm proximally from the distalmost end. In posterior view, the ventral and dorsal margins are concave, the former of which is more deeply curved. The distal condyles are flatter in the right humerus that results in a weakly convex distal margin. The ulnar and radial condyle are separated by a flat depression that extends for approximately 147 mm in a proximal direction as a shallow indentation across the posterior surface. The ulnar condyle is the larger of the two and is mediodistally flattened, showing a well-developed entepicondyle that slopes approximately 55° proximomedially and has an anteroproximally-posterodistally concave surface (Fig. 13C and D).

Radii—Both radii are preserved in articulation, with both of them contacting the humerus at their proximal ends and the carpus at their distal ends. The shafts and distal ends are medially exposed in both radii. The proximal end is visible only in the right radius due to the superimposed left ulna covering the proximal third of the left radius (Fig. 13). The right radius is slightly longer (255 mm) than the left (245 mm).

The shafts of both radii are subelliptical in cross-section and are gracile and fairly straight. The right radius is the flatter of the two. The radii are slimmest anteroposteriorly below the midshaft, with diameters of 44 mm (right) and 42 mm (left). Both radii are also anteroposteriorly expanded towards both ends which may be due to post-depositional compaction (Fig. 13). The right radius is anteroposteriorly widest at its proximal end at around 71 mm, while the left radius does not show this feature (Fig. 13). The proximal end of the right radius has a posterodorsally orientated, weakly concave, articular surface with prominent margins. The distal ends are elliptical in cross-section, with diameters along their long axes of 63 mm and 58 mm for the left and right radii, respectively. The right radius has a flatter distal surface than the left and features a shallow anteroposterior groove.

Ulnae—The ulnae are preserved in articulation with the radii and only show minor degrees of compaction (Fig. 13). The total proximodistal lengths of these elements are 300 mm and 285 mm for the right and left ulnae, respectively.

In both ulnae the lateral margins are more convex than their medial margins, and the midshafts are elliptical (Fig. 13). A shallow indentation is present on the medial surfaces that is more prominent in a distal–proximal direction. This indentation is best seen in the left ulna, which starts around 50 mm from the distal margin and exhibits a maximum width of around 55 mm approximately 28 mm below the proximal margin. The expanded proximal heads are triangular in section, bearing concave radial fossae. Both the olecranon process and olecranon basins are well-developed. Distally, the shafts decrease in both anteroposterior width and mediolateral thickness before reaching minimum widths of 52 mm and 45 mm (right and left, respectively), around 65 mm proximal to the distal ends. The distal ends are anteroposteriorly wider at 80 mm and 70 mm (left and right, respectively) and have elliptical-shaped convex distal surfaces.

Manus—Both manus are almost entirely preserved in palmar view and are fully articulated with the respective antebrachium. The manus exhibit maximum lengths of 275 mm and 270 mm for the left and right manus, respectively (Table 4). The left manus comprises complete digits I–III but digits IV and V are both missing their distalmost phalanges (mp IV-3 and mp V-3). In the right manus, only the distalmost phalanx of digit V (mp V-3) is absent. In both manus, all three unguals are preserved, as well as all five metacarpals and all three carpals.

Carpals—Each manus comprises three carpals assigned to distal carpals I–III. However, overlaying matrix and poor preservation make identification of morphological details challenging, especially for smaller elements.

Distal carpal I is the longest carpal bone with maximum radioulnar lengths of 52 mm and 46 mm (right and left, respectively). In palmar view, the left element is subrectangular, while the right is more subtriangular and slightly curved (Fig. 14). Both elements are elongated in a radioulnar direction and are weakly convex on their palmar surfaces.

Distal carpal II is the second largest carpal in the manus, with maximum radioulnar lengths of 36 mm and 33 mm (left and right, respectively) and maximum proximodistal lengths of 20 mm and 18 mm (left and right, respectively). In the left manus, distal carpal II is located on the ulnar side of distal carpal I, while in the right manus, this element is situated proximal to distal carpal I. In palmar view, both elements are subelliptical with mostly flat palmar surfaces (Fig. 14).

The distal carpals III are located on the immediate ulnar side of the distal carpals II, distal to the ulnae and proximal to the metacarpals III. Although the left distal carpal III is mostly indiscernible, the right distal carpal III is somewhat triangular in palmar view with a maximum diameter of 26 mm and a flat palmar surface (Fig. 14).

Metacarpals—In both manus, all five metacarpals are preserved in articulation, contacting the carpals distally and the phalanges proximally. In the left manus, metacarpals I–IV are situated parallel to each other and contact the adjacent elements both laterally and medially, while metacarpal V is abducted. In contrast, in the right manus metacarpals I–V are positioned in a curved pattern with metacarpal IV laying on top of metacarpal-I (Fig. 14). Despite being well-preserved with only minor cracks present, most of the radioulnar articulation surfaces are at least partially obscured by the superimposition of adjacent bones.

Metacarpal I is the largest bone of the manus with a maximum transversal width of 60 mm and 50 mm in the left and right manus, respectively (Table 4). These elements are subrectangular in palmar view with proximal width/total length ratios of 1.4. The cross-sections are subrectangular in proximal view. In palmar

Table 4 Metacarpal and manual phalanges of the left and right manus of *Plateosaurus trossingensis* NMZ 1000001

Manus	max. L		art. L		prox. W		dist. W	
	Left	Right	Left	Right	Left	Right	Left	Right
mc I	80	78	52	55	60	50	57	~58
mc II	100	105	~98	~100	>44	>35	~55	45
mc III	95	100	~93	~94	56	>31	~32	~32
mc IV	78	79	75	>67	41	33	24	~20
mc V	40	>34	37	~28	31	35	~18	28
mp I-1	68	69	~65	60	57	56	~50	48
mp I-2 (un I)	114	114	93	84	~16	>18	-	-
mp II-1	~55	64	>45	46	52	43	47	42
mp II-2	~53	59	>36	>40	43	42	42	~36
mp II-3 (un II)	83	86	69	71	27	>10	–	–
mp III-1	43	56	~37	36	>33	~32	~35	27
mp III-2	38	>40	25	~29	~32	29	24	25
mp III-3	36	42	22	28	24	22	>17	>17
mp III-4 (un III)	64	62	57	50	12	>11	–	–
mp IV-1	25	28	>23	19	>25	20	~18	~17
mp IV-2	21	20	17	~17	>10	15	~9	~7
mp IV-3	–	12	–	~10	–	~10	–	6
mp V-1 + mp V-2	24	~22	23	>18	25	~20	15	~10

art. L. length between proximal and distal articular surfaces, *dist. W.* maximum radioulnar width measured at the distal end, *mc* metacarpal, *max. L.* maximum proximodistal length, *mp* manual phalanx, *prox. W* maximum radioulnar width measured at the proximal end, *un* ungual. All measurements in mm

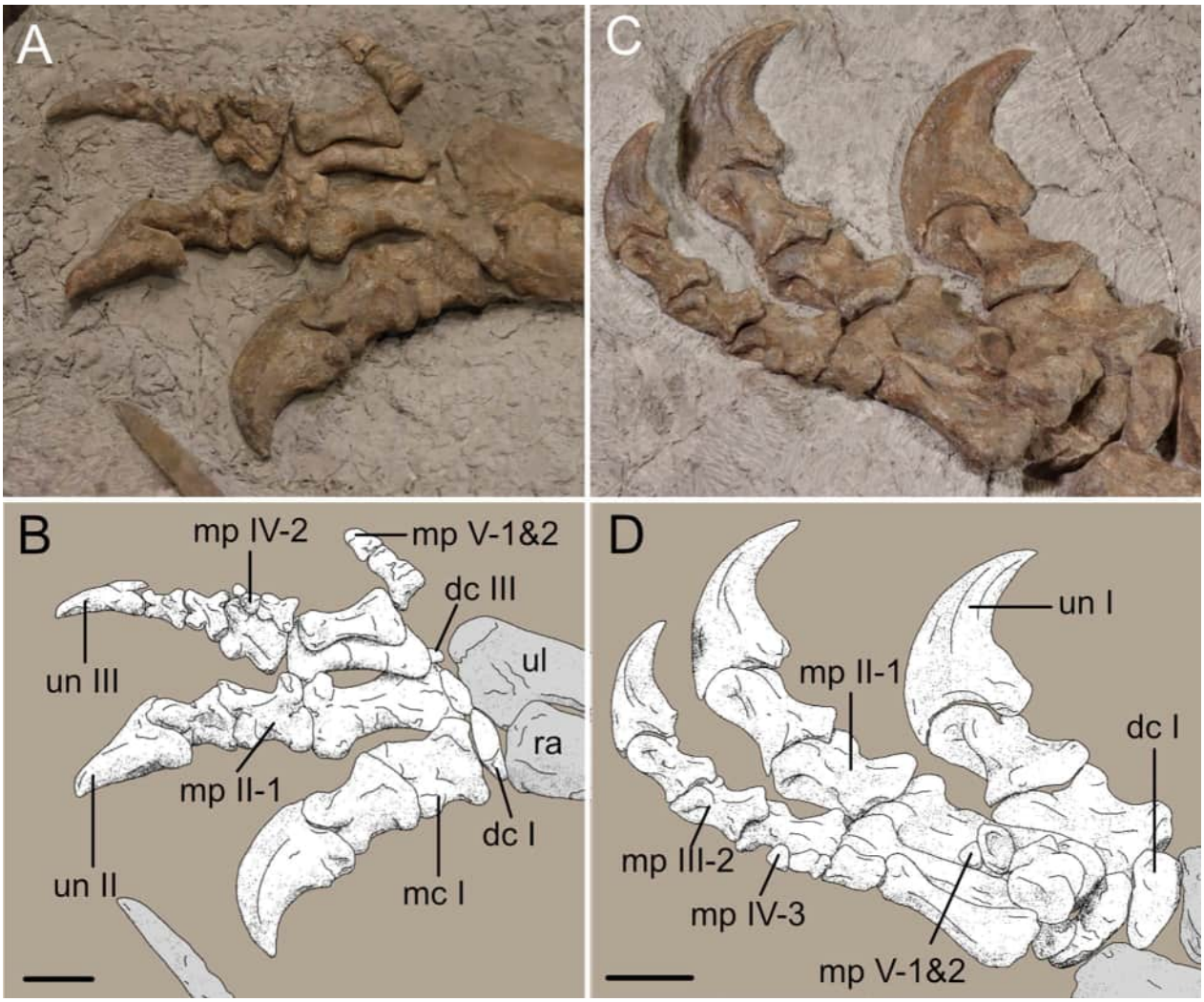

Fig. 14 Manus of *Plateosaurus trossingensis* NMZ 1000001. **A** photograph and **B** interpretive drawing of the left manus in palmar view. **C** photograph and **D** interpretive drawing of the right manus in palmar view. *dc* distal carpal, *mc* metacarpal, *mp* manual phalanx, *ra* radius, *ul* ulna, *un* ungual. Scale bars 50 mm

view, the proximal margin of the left metacarpal I is weakly concave, while the margin is flat in the right. The distal articular surface bears a prominent central groove termed the intercondylar sulcus, which fits the corresponding articulating facet of the distalmost phalange of the digit. The intercondylar sulcus is delimited by a well-developed medial condyle and a weakly developed lateral condyle, resulting in a slightly medially orientated abduction of digit I in a neural manus posture relative to digits II–IV (Fig. 14).

In a proximodistal direction, both metacarpals II and III are around 1.3 times longer than metacarpal I, while metacarpals IV and V are of similar length and 0.4 times the length of metacarpal I (Table 4). As the width of the shafts decrease across the metacarpals, the mid-shaft constriction becomes progressively more prominent from metacarpals I to IV, with metacarpal V exhibiting weak mid-shaft constriction. The shaft cross-sections are more subelliptical in metacarpals II and III but are more trapezoidal in metacarpals IV and V (Fig. 14).

In metacarpals II–V, the dorsally exposed palmar surfaces appear slightly concave and are delimited by prominent margins of the proximal and distal articular surfaces (Fig. 14). Similar to metacarpal I, the proximal articular surfaces of the subsequent metacarpals are weakly convex in metacarpals I–IV with a rounded trapezoidal shaped cross-section, while that of metacarpal V is mostly flat in both manus (Fig. 14). The intercondylar sulcus decreases in prominence on subsequent metacarpals so that it is noticeably shallower

in metacarpals II and III, weakly developed in metacarpal IV and is absent in metacarpal V. In the left manus, the distal articular surface of metacarpal V appears convex.

Manual phalanges—The phalangeal formula in Plateosaurus is 2/3/4/3/3, with the three inner digits terminating in claw-bearing unguals (Huene, 1926). In both manus, all five digits are fully articulated. While the proximal phalanges are generally well-preserved, the distal phalanges are more poorly preserved, with the left manual phalange IV-3 and the left and right manual phalange V-3 not preserved at all.

Digit I comprises two phalanges, a proximal non-ungual phalanx (manual phalanx I-1) and a distal ungual (manual phalanx I-2, ungual I). Manual phalanx I-1 is the largest and most robust phalanx in the *Plateosaurus* manus, measuring 68.5 mm long and 56.5 mm wide (Table 4). The proximal articular surface of manual phalanx I-1 is strongly concave and features a central dorsopalmar ridge, allowing close articulation with the intercondylar sulcus of the metacarpal, while its distal end bears a concave articulation facet that matches the convex proximal facet of ungual II, the distal ungual of digit II.

Non-ungual phalanges of digits II–V are similar to digit I in terms of shape, but they are smaller and somewhat longer in proximodistal extent. Manual phalanges V-1 and V-2 are fused (Fig. 14). The proximal end of the distal phalanges is convex and has a central crest that articulates with the grooved distal end of the proximal phalanges.

The distalmost phalanges of digits I–III are claw-bearing unguals that gradually decrease in size in the ulnar direction (Table 4). Ungual I is approximately 1.3 and 1.2 times longer than ungual II in proximodistal and anteroposterior directions, respectively, and is 1.8 and 2 times longer than ungual III. The proximal articular surfaces are saddle-shaped and strongly concave. In all three unguals of both manus, the flexor tubercles are well-defined but small. The outer curvature is similar between the three elements, while the inner curvature is weaker in ungual I and increases in unguals II and III. In each ungual the medial surface is transversed by two grooves, a dorsal and central one, which converge approximately two-thirds distal to the proximal margin before disappearing shortly after. Ventral to the central groove, a prominent eminence extends parallel along the inner curvature and terminates just below the distal tip (Fig. 14).

Pelvic girdle

The pelvic girdle comprises the left and right ilia, the posterior portions of both pubes (including the posterodorsal surface of the right pubis) and a small posterior portion of the left ischium.

Ilia—Both ilia are well-preserved in close contact with the pubes and sacral vertebrae (Fig. 15A and B). The dorsal surfaces and dorsal halves of the lateral surfaces are exposed, while most of the medial surfaces and the entire ventral surfaces are obscured by matrix (Fig. 15A and B). In dorsal view, the illium is sigmoidal in shape with a posterolaterally-orientated postacetabular process and a transversely constricted iliac blade. The dorsal margin is slightly convex except for a minor indentation caused by the projection of the preacetabular process in the anterolateral direction. In contrast to the short, subtriangular preacetabular process (ca. 75 mm long), the postacetabular process is mediolaterally longer (ca. 340 mm; Fig. 15A and B). The posterior end of the postacetabular process is mediolaterally enlarged, with a slightly convex posterior margin in lateral view and a straight margin in dorsal view. Both the pre- and postacetabular processes on their lateral surfaces bear weakly developed striations in an anteroposterior direction. Ventral to the mediolateral constriction of the iliac blade, a well-developed supraacetabular crest extends anteriorly into an elongated pubic peduncle. In dorsal view, the lateral margin of the pubic peduncle is weakly sinuous in shape while the medial margin is straight. The anteroventrally-oblique articular surface of the pubic peduncle has a diameter of ca. 112 mm (left) and 108 mm (right). The right peduncle is missing a piece of the anteromedial margin. The articular surface of the left peduncle appears convex but is mostly flat in the right peduncle.

Pubes—Both the left and right pubes are preserved in situ with the anterior side facing upwards and are situated lateral and lateroventral to dorsal vertebrae 12–15 (Fig. 15C and D). For both bones, only the posterior halves of the pubic aprons are exposed, while the articulations with the ilium and ischium at the proximal ends, are buried in sediment or covered by other bones.

The left and right pubic shafts are both flat and have maximum proximodistal lengths of ca. 290 mm and 390 mm, respectively, as exposed in the matrix. The medial and lateral margins are roughly parallel and continue mostly straight anteriorly. The anteroposteriorly expanded iliac peduncles are larger in their mediolateral than dorsolateral extent, with the dorsal surface faintly striated in a proximodistal direction.

Ischium—The left ischium is represented by the distal half of the posteriorly-directed ischiadic shaft with only the left lateral surface exposed (Fig. 15E and F). The element is generally well-preserved and shows no sign of damage. It is located central to caudal vertebrae 1 and 2

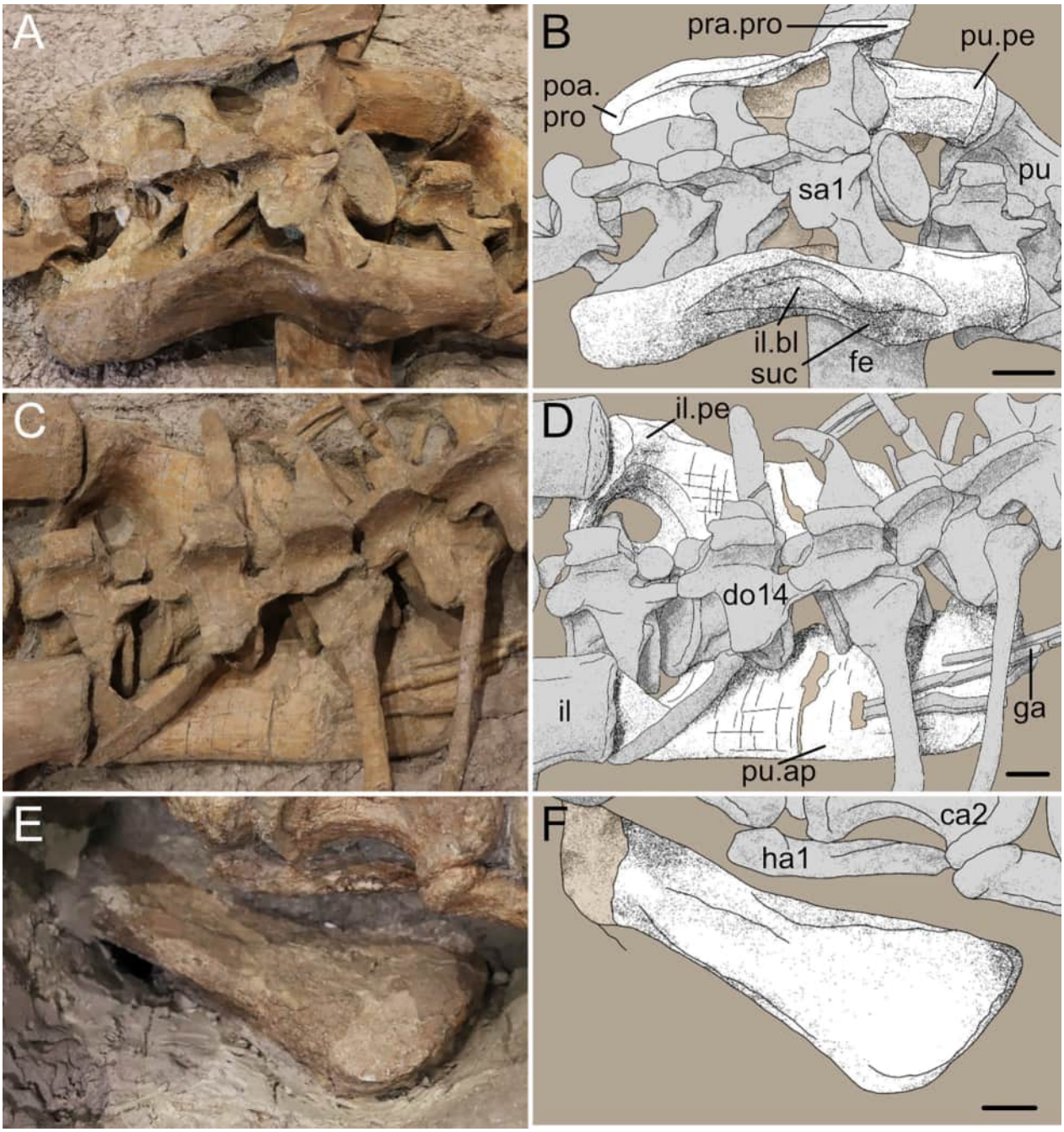

Fig. 15 Pelvic bones of *Plateosaurus trossingensis* NMZ 1000001. **A** photograph and **B** interpretive drawing of the right ilia in laterodorsal view. **C** photograph and **D** interpretive drawing of the pubis in anterior view. **E** photograph and **F** interpretive drawing of the left ischium in lateral view. *ca* caudal vertebra, *do* dorsal vertebra, *fe* femur, *ga* gastralia, *ha* haemal arch, *il.bl* iliac blade, *il.pe* ilium peduncle, *poa.pro* postacetabular process, *pra.pro* preacetabular process, *pu* pubis, *pu.ap* pubic apron, *pu.pe* pubic peduncle, *sa* sacral vertebra, *suc* supraacetabular crest. Scale bars 70 mm (**A**, **B**), 40 mm (**C**, **D**) and 30 mm (**E**, **F**)

(Fig. 15E and F). The visible part of the ischium measures approximately 170 mm in length and the proximal shaft is 53 mm wide. The shaft extends mostly straight distally before expanding in dorsoventrally into an ischial boot that reaches a maximum height of 73 mm. The

posterior margin of the distal end is weakly convex and anteroventrally oblique.

Hindlimb

The left and right hindlimbs are preserved in articulation and are situated on the lateral sides of the pelvic girdle (Fig. 16). The right hindlimb is outstretched laterally, with the femur and pes orientated slightly anterolaterally and the lower limb pointing posterolaterally (Fig. 16C and D). The exposed part of the hindlimbs have proximodistal lengths of ca. 188 cm (left) and 192 cm (right).

Femora—Both femora are well-preserved and exposed anteriorly, articulating with the pelvic girdle at their proximal ends and with the tibia and fibula at their distal ends. A few post-depositional fractures are present on the surfaces of both femora. The femoral heads are mostly concealed by the sacrum with the femoral shafts appearing sigmoidal in anterior, posterior and lateral views. The total proximodistal length of each femur is 780 mm (measured by BP during the original excavation and disassembly of the specimen), with exposed lengths of approximately 680 mm and 660 mm for the left and right femur respectively.

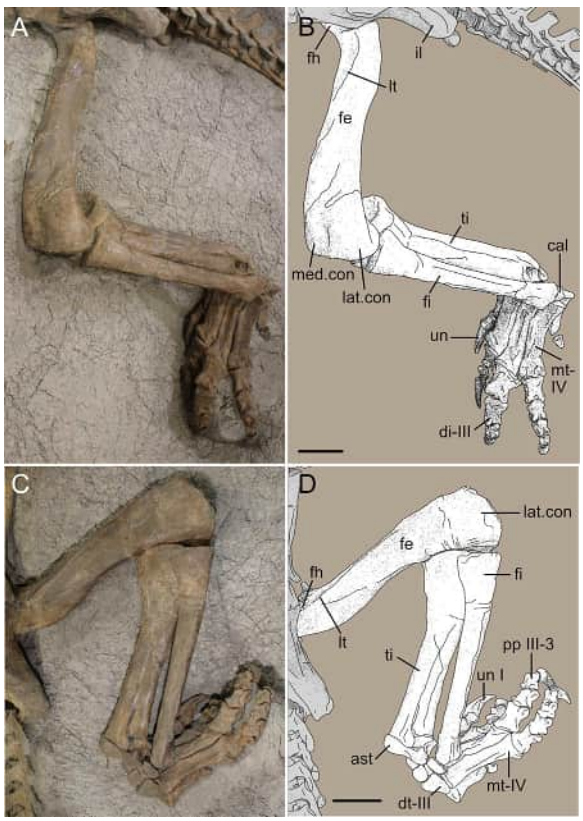

Fig. 16 Hindlimbs of *Plateosaurus trossingensis* NMZ 1000001. **A** photograph and **B** interpretive drawing of the left hindlimb in lateral view. **C** photograph and **D** interpretive drawing of the right hindlimb in dorsal view. *ast* astragalus, *cal* calcaneus, *di* digit, *dt* distal tarsal, *fe* femur, *fh* femoral head, *fi* fibula, *il* ilum, *lat.con* lateral condyle, *lt* lesser trochanter, *med.con* medial condyle, *mt* metatarsal, *pp* pedal phalanx, *ti* tibia, *un* ungual. Scale bars 10 cm

Below the femoral head on the anterior surface is a weakly curved crest that forms the faintly convex lesser trochanter (Fig. 16). The anteroposteriorly thinnest point of the femoral shaft is located right below the presumed location of the fourth trochanter, measuring 114 mm and 120 mm in the left and right femur, respectively. The distal margin is slightly convex in anterior view and features a smaller, less pronounced medial condyle and a larger well-developed lateral condyle.

Tibiae—Both tibiae are generally well-preserved and articulated with the femora proximally, the fibulae laterally and the astragalus distally. The left tibia is exposed posterolaterally while the right tibia is mostly laterally exposed (Fig. 16). The cnemial crests of the bones are largely hidden in the matrix. The tibiae are relatively straight with maximum proximodistal lengths of around 570 mm and 560 mm for the left and right elements, respectively. The midshaft cross-section is subtriangular with the proximal ends exhibiting a more triangular-shaped cross-section, with maximum widths of 210 mm (right) and 205 mm (left). As seen in the left tibia, the laterally oblique proximal head is divided into a concave medial surface and a posterolaterally-orientated external condyle (Fig. 16). The articular surface of the external condyle is subcircular in cross-section.

The distal condyles are slightly mediolaterally expanded with maximum widths of around 66 mm (left) and 63 mm (right). Distally, the left tibia is anteriorly expanded in the metaphyseal region. The articular surface features a central depression, separating the weakly-developed anterior process from the more prominent posterior process. The depression extends onto the lateral surface of the distal end in the form of a 95 mm long groove. In the right tibia, the distal articular surfaces are obscured by the close articulation with the tarsus. The proximally extending groove is clearly exposed and has a maximum length of 110 mm before ending on the lateral surface of the shaft.

Fibulae—The fibulae are preserved in articulation with the femora proximally and with the tarsi distally. The lateral surfaces of the elements face upwards (Fig. 16). The fibulae are thin and gracile with proximodistal lengths of 540 mm (left) and 560 mm (right). The fibular shafts are elliptical in cross-section with minimum anteroposterior and mediolateral extents of around 53 mm and 35 mm, respectively. The fibular shafts are straight in lateral view but are weakly curved in anterior and posterior views and exhibit a lateral convexity in their proximal halves. The fibulae are widest at their proximal ends with 125 mm

(left) and 108 mm (right). The proximal heads are slightly tilted anteriorly and bear flat articular surfaces. The distal ends, in contrast, are weakly anteroposteriorly expanded and have subelliptical cross-sections. Due to the poor preservation of the distal ends and close articulations with the calcanei, the distal articular surfaces are mostly indiscernible on both sides.

Pedes—Both pedes are preserved in full articulation with their respective tibia and fibula (Figs. 16 and 17). The central elements are mostly visible from their dorsal surfaces while the medial most metatarsal and phalanges are also visible from medial and lateral views. The maximum preserved lengths of the left and right pes are 550 mm and 500 mm, respectively. This size difference is believed to be due to taphonomic shortening of the right pes since some elements of Frick *Plateosaurus* can be up to 30% shorter than their counterparts (B. Pabst, pers. obs.).

Tarsals—The proximal tarsal row comprising the astragalus and calcaneus is fully preserved in both pedes and are situated in close articulation with the tibia and fibula (Figs. 16 and 17). In the left pes, both elements are mostly posteriorly and slightly distally exposed, while in the right pes they are exposed more distally than posteriorly. Another small bone fragment, most likely part of a distal tarsal, is preserved in the right pes but its identification is not definitive due to its size and indistinct morphology.

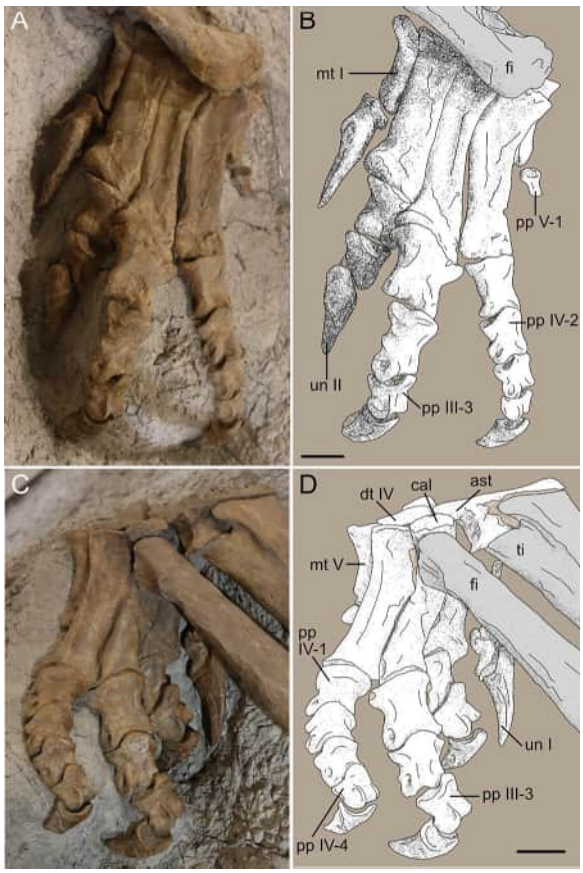

Fig. 17 Pes of *Plateosaurus trossingensis* NMZ 1000001. **A** photograph and **B** interpretive drawing of left pes in dorsal view. **C** photograph and **D** interpretive drawing of the right pes in dorsal view. *ast* astragalus, *cal* calcaneus, *dt* distal tarsal, *fi* fibula, *mt* metatarsal, *pp* pedal phalanx, *ti* tibia, *un* ungual. Scale bars 40 mm

The astragali are the largest elements of the tarsus with approximate mediolateral widths of 132 mm and 120 mm in the right and left pes, respectively (Fig. 17). In distal view they are wing-like in shape with an enlarged convex medial portion and a subrectangular portion that has a convex medial edge. The distal articular surface is strongly concave. The thickest part of the astragali proximodistally is at the anteromedial apex of the ascending process that measures approximately 83 mm and 70 mm in the right and left astragalus, respectively. The calcaneal articular surface is concave while the proximal articular surface is mostly obscured due to it being in close articulation with the tibia. In posterior view, the proximal margin is convex.

The right calcaneus is slightly smaller than the left, with the former measuring 65 mm in height and 44 mm in width, and the latter measuring 52 mm and 35 mm in height and width, respectively (all measurements as exposed). Both calcanei are subrectangular in posterior view and distally the left is subovoid while the right appears somewhat 'duck-bill' shaped (Fig. 17). The distal articular surface is weakly convex and delimited by prominent margins, while the proximal articular surface is only partly visible, appearing slightly concave in posterior view.

In the right pes distal tarsal II is preserved in articulation with metatarsal II and is proximally exposed. It is subrectangular in shape and measures 60 mm by 43 mm anteroposteriorly and mediolaterally, respectively. Posteriorly the tarsal is mostly flat. The anterolateral corner of the proximal articular surface is notably more concave.

Both distal tarsals III are proximally exposed and are preserved in close articulation with metatarsal III. The left tarsal III has a maximum mediolateral width of 48 mm while the right is slightly larger with 54 mm. Tarsal III is subrectangular with rounded corners and a weakly concave proximal articular surface.

Only the right pes has a preserved distal tarsal IV, which is situated laterally to digit III and is exposed proximally (Fig. 17C and D). It is the largest tarsal in the distal row, measuring 63 mm mediolaterally and 60 mm anteroposteriorly, and has a rounded triangular shape in proximal view. The articular surface is mostly flat but bulges slightly towards the posterior margin.

Metatarsals—In each pes, all five metatarsals are preserved in articulation with close articulations of the metatarsophalangeal joints obscuring the distal articular facets. The left metatarsals are better preserved than the right and the right metatarsal I is partially obscured by superimposed tarsals and the proximal ends of both the tibia and fibulae. The proximal halves of right metatarsals II and III are mostly covered by the fibular distal end. In both pedes, metatarsals I–IV are situated parallel to each other, while metatarsal V is slightly abducted laterally in the left pes and is partially overlaid by metatarsal IV in the right pes. Metatarsals II–IV are longer and more robust than metatarsals I and V (Fig. 17).

Metatarsal I is the shortest at around 110 mm and 90 mm long in the left and right pes, respectively. This size difference is believed to be taphonomic shortening of the right element. In the left pes, the shaft of metatarsal I is slightly slimmer than the other metatarsals and expands mediolaterally towards its proximal end. When viewed anterodorsally, the proximal articular facets are mostly flat.

Metatarsal II is approximately 1.8 times longer than metatarsal I while the longest metatarsal, metatarsal III, is around 2.3 times longer than metatarsal I with a length of around 250 mm. The shafts of metatarsals II and III are subrectangular in section and extend mediolaterally towards the proximal and distal ends. The proximal articular facets of both elements are not visible, while the distal articular facets are only partially visible and are possibly slightly convex.

The lengths of metatarsals IV and V are approximately 2.1 and 1.3 times that of metatarsal I, respectively. The shafts of these two elements are flatter and more rectangular than those of metatarsals II and III. Mediolateral expansion of the distal ends is present in metatarsal IV but not in V. The proximal articular surfaces are mostly flat with a shallow central groove in the left IV and a concavity in the right IV. The distal articular facets are slightly more convex than in other metatarsals.

Pedal phalanges—Each pes comprises 15 preserved articulated phalanges corresponding to the pedal formula of *Plateosaurus* (2/3/4/5/1), with the distal-most phalanges of digits I–IV representing claw-bearing unguals (Huene, 1926; Mallison, 2010a). The digits are preserved in close articulation with both the metatarsals and each other, leaving most of the phalangeal proximal and distal articular facets are at least partially obscured. Both pedes exhibit a degree of digit spreading, exposing the phalanges not only dorsally but also medially and laterally (Fig. 17). The pedal unguals are only partially visible due to the position of the digits. Digit III is the longest with a proximodistal length of around 300 mm, followed by digits IV, II and I with the reduced digit V being only around 42% as long as digit III (Table 5).

The proximalmost phalanx of digit III is the largest element of the phalangeal series with proximodistal and mediolateral lengths of 90 mm and 92 mm, respectively, in the left pes. In each digit, the proximal phalanx is the most robust while distally, the phalanges diminish in both size and robustness (Table 5).

The proximal articular facets of all proximal phalanges (pp I-1 to pp V-1) are strongly convex while in the more distal phalanges, they have saddle-shaped articular facets with well-developed dorsal margins. The distal articulations are concave medially to allow close articulation of the phalangeal joints. The distal ends are marked by deep depressions on their medial and lateral surfaces. However, both pp V-2 and pp V-3 are missing in both pedes.

The general morphology of unguals II–IV is similar to that of ungual I but they decrease in size in a lateral direction (Fig. 17). The maximum length of ungual I is 140 mm and 130 mm in the right and left pes, respectively. The strongly convex articular surface is enclosed by a thin but distinct proximal margin, and the lateral surface is traversed by a well-defined groove from the distal tip to the ventral margin of the weakly-developed flexor tubercules.

Unidentified bone fragments

There are two unidentified bone fragments in the abdominal region which are present in their original positions (Figs. 6 and 18). The largest fragment is partially obscured by dorsal rib 12, is subrectangular with curved lateral and medial edges, and measures approximately 40 by 75 mm (exposed view; Fig. 6). This fragment is quite poorly preserved and partially covered in artificial matrix (Fig. 6). The second, smaller fragment is partially covered by dorsal vertebra 11, is flat and rectangular, and measures approximately 30 mm by 55 mm (exposed view; Figs. 6 and 18). This fragment is generally well preserved except for partial damage on its posterolateral edge (Fig. 18). Based on its appearance and location, it is possible this fragment could represent the distal end of a dorsal rib. The possibility that these fragments represent stomach contents is being investigated.

Pectoral and upper forelimb pathological tissue of NMZ 1000001 and comparison with SMF 11.4

The pathology mostly affects the right scapula and humerus (Figs. 11, 13, 19, 20 and 21). It forms an irregularly shaped cluster of bone with a very rugose surface texture, completely obscuring any morphological properties in the distal half of the scapular shaft and the proximal half of the humerus. The pathological tissue

Table 5 Metatarsal and pedal phalanges of the left and right pedes of *Plateosaurus trossingensis* NMZ 1000001

Pes	max. L		prox. W		dist. W	
	Left	Right	Left	Right	Left	Right
mt I	> 110	> 90	–	–	55	–
mt II	200	–	~ 90	–	75	–
mt III	–	250	85	–	85	70
mt IV	225	210	~ 70	–	65	70
mt V	145	130	75	–	20	~ 30
pp I-1	55	–	55	–	45	–
pp I-2 (un I)	130	140	> 35	50	–	–
pp II-1	> 65	60	~ 60	60	45	50
pp II-2	> 60	50		55	40	45
pp II-3 (un II)	130	> 100	31	35	–	–
pp III-1	85	80	90	80	70	60
pp III-2	75	60	70	60	45	50
pp III-3	50	50	45	40	35	40
pp III-4 (un III)	90	110	~ 35	35	–	–
pp IV-1	70	75	70	65	~ 60	55
pp IV-2	58	55	50	55	45	45
pp IV-3	40	50	35	50	45	40
pp IV-4	40	37	35	40	30	30
pp IV-5 (un IV)	~ 90	75	30	25	–	–
pp V-1	35	35	35	30	–	–

dist. W. maximum mediolateral width measured at the distal end, *max. L.* maximum proximodistal length, *mt* metatarsal, *pp* pedal phalanx, *prox. W* maximum mediolateral width measured at the proximal end, *un* ungual. All measurements in mm

extends beyond the original bone margins, making it difficult to distinguish between individual elements in external view. The scapula head, while still identifiable, is detached from the rest of the scapula (Figs. 11 and 19) as a result of a proliferate bone reaction. There is a large, irregularly shaped infectious process (i.e., a bony protrusion) between the proximal-posterior section of the humerus and the proximal half of the scapula that has fused these bones together (Figs. 19 and 20). There is also a small degree of fusion between the antero-proximal part of the scapula and the dorsolateral corner of the coracoid (Fig. 21). The transition from pathological to normal tissue varies between bones, with the transition being abrupt in the scapula, and mostly gradual in the humerus (Figs. 19, 20 and 21). CT-scanning further highlights the large infectious processes and high degree of fusion between the humerus and scapula (Fig. 20) and, to a lesser extent, between the scapula and coracoid (Fig. 21). The scans reveal that the internal bone structures of the humerus and scapula have also been extensively remodelled where the pathological material is present externally (Figs. 20 and 21). For example, in the humerus, the medullary cavity in the diaphyseal region is irregular with pathologically thickened cortical bone extending into the medullary region (Fig. 20). The CT-scans also show that the cortices the epiphyseal regions of the pathological right humerus and the non-pathological left humerus are extremely thin and tapering towards the epiphyses (Fig. 20D). In the shaft region, humeral cortical thickness is larger and the distinction between cortex and internal cancellous tissue in the medullary region is usually distinct (Fig. 20D, K, L).

In comparison, the left radius and ulna of SMF 11.4 that also show pathological material exhibit very different external and internal structures from both the pathological material of NMZ 1000001 and from the normal right radius and ulna of SMF 11.4 (Figs. 22, S2 and S3). The left elements of SMF 11.4 are both altered in their external morphology. They are lateromedially flattened, with their midshafts being more elliptical in shape in contrast to the subcircular midshafts of the right pair (Figs. 22 and S3). The proximal and distal margins of the left radius, and the distal margin of the left ulna, are also very lateromedially flattened and elliptical in shape (Figs. 22 and S3). In contrast, the proximal margin of the left ulna has a lateromedially flattened posterior process but an enlarged and more rounded anteromedial process, relative to that of the right ulna (Figs. 22 and S3). The distal half of the left ulna also has a very pronounced medial curvature not observed in the right

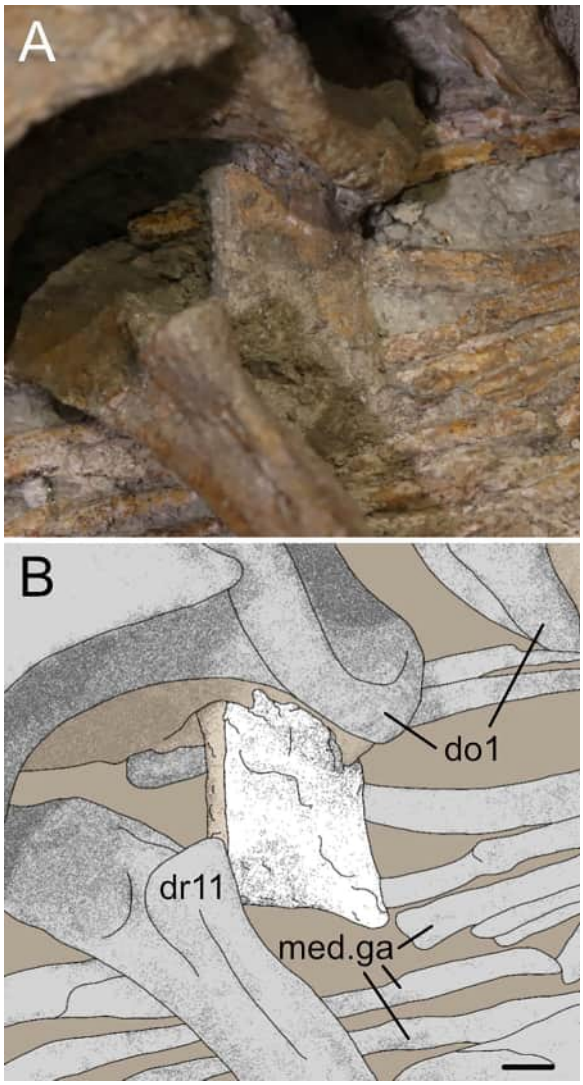

Fig. 18 Unidentified bone fragment from *Plateosaurus trossingensis* NMZ 1000001. **A** photograph and **B** interpretive drawing of an unknown bone fragment under the centrum of the eleventh dorsal vertebra. *do* dorsal vertebra, *dr* dorsal rib, *med. ga* medial gastralia. Scale bars 10 mm

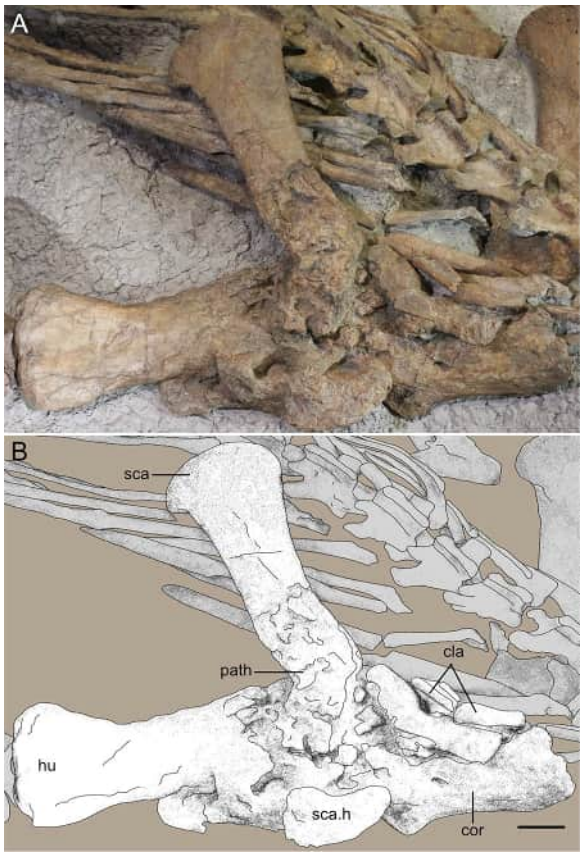

Fig. 19 Right pectoral girdle with pathological tissue of *Plateosaurus trossingensis* NMZ 1000001. **A** photograph and **B** interpretive drawing of the scapula, coracoid, clavicle, humerus and pathological tissue. *cla* clavicle, *cor* coracoid, *h* head, *hu* humerus, *path* pathological tissue, *sca* scapula. Scale bars 50 mm

radius (Figs. 22 and S3). The left radius has two large potential neoplasms on the medial and anterior surfaces of the midshaft (Figs. 22 and S3). The medial neoplasm is the largest and measures 64 mm along its proximal–distal axis, 33.5 mm along its anterior–posterior axis at its widest point, and 8 mm high from the medial surface. The neoplasm has a distinct proximal boundary with a sharp raised edge and thick anterior and posterior edges, as revealed by CT-scanning (Figs. 22 and S3). The anterior neoplasm measures 58 mm along its proximal–distal axis, 18 mm along its anterior–posterior axis at its widest point and 10 mm along its lateral-medial axis at its widest point (Fig. 22A). This neoplasm also has a small circular bony nodule protruding from near its proximal margin (Fig. 22A). The left radius also has very thin cortical bone at its lateral margin at the midshaft opposite the medial neoplasm, in contrast to the thick cortical bone at the midshaft of the right radius (Fig. 22B, D).

The left ulna has one large callus (a highly vascular overgrowth of woven bone that envelopes a fractured area; Bertozzo et al., 2023, 2024) that is mostly visible from its lateral surface but is also visible on the medial surface as a slight bulging of the surface in the approximate mid-section of the shaft (along both anteroposterior and proximodistal axes; Figs. 22 and S3). The callus measures 54.5 mm along its proximal–distal axis, measured from the lateral surface, 30 mm along its anterior–posterior axis at its widest point on the lateral surface and 33.5 mm along its lateral-medial axis, measured between the lateral and medial surfaces (Fig. 22C). The callus has a distinct distal boundary

with a sharp raised edge but with thinner anterior and posterior cortical bone than the left radius medial callus (Fig. 22). Internally, the left ulna has thin cortical bone at the midshaft along its lateral and posterior margins, similar to the left radius (Fig. 22). However, the internal margin of the cortical bone at the medial surface is very indistinct in contrast to the sharp boundary observed from the left radius (Fig. 22B and F). There is also a 'ring' of internal bone located just medial to the visible callus on the lateral surface (Fig. 22F). The full osteological description of the radius and ulna of SMF 11.4 can be found in the supplementary information.

Body size estimation of NMZ 1000001

The missing skull and cervical series of NMZ 1000001 unfortunately prevents a direct snout-to-tail measurement of the specimen. However, using the total femur length of 78 cm, and the femur/body length ratio of 1:10 from Sander (1992), we estimate that NMZ 1000001 had a total body length of around 7.7–7.8 m.

Histological description of NMZ 1000001

Dorsal rib 7

The dimensions of the thin sectioned part of dorsal rib 7, taken roughly from the mid-shaft region of the rib, are approximately 17 mm and 7 mm, which corresponds to the maximum lengths along the anteromedial-posterolateral and anterolateral-posteromedial axes, respectively (Fig. 23). In transverse section, the bone is subtrapezoidal and slightly dorsoventrally flattened. Apart from a missing piece of bone at the anterior corner, the cross-section is rather complete and is generally well-preserved.

The microanatomy of the internal rib shaft region of sauropodomorph ribs is similar to that of long bones, with an outer cortical compact bone (cortex), an inner spongy cancellous area and, potentially, a medullary cavity (Waskow & Sander, 2014). In dorsal rib 7, the medullary region is filled by a bony trabecular network. The bone trabeculae appear secondarily remodelled and consist of lamellar bone. The perimedullary region contains several large resorption cavities, some of which are filled with minerals while others are empty. The size of the resorption cavities generally decreases from the medullary region to the inner cortex and the cancellous bone gradually transitions to the inner cortex without sharp boundary. The thickness of the cortex surrounding the rib shaft varies, with the thickest part being found at the posterior side of the rib. The primary bone tissue consists mostly of woven-parallel complex (Buffrénil & Quilhac, 2021), dominated by a parallel-fibred matrix well vascularized with longitudinal osteons, but in the process of becoming further remodelled by a high number of scattered secondary osteons. Primary bone tissue is thus only preserved in some regions of the bone as most of the inner and outer cortex is already highly remodelled.

As the extent of bone resorption and remodelling decreases from the inner cortex to the surface, secondary osteons are generally larger in the inner cortical than outer cortical layers (Fig. 23). Most of the remodelled bone tissue is around the anteromedial and posteromedial sides, while anterolateral and posterolateral sides preserve more primary bone tissue. Although the primary bone tissue of the dorsal surface exhibits several wider-spaced lines of arrested growth (LAGs) and an external fundamental system (EFS sensu Woodward et al., 2011, = outer circumferential layer sensu Ponton et al., 2004; Fig. 23), it is not possible to reconstruct the growth record from this sample, as most of the inner growth lines have been at least partially replaced with Haversian bone (likely due to the position of the section at mid-rib; see Waskow & Sander, 2014). Polarised light reveals Sharpey's fibres on the anteromedial and posteromedial external surfaces, indicating insertion areas for intercostal muscles.

(See figure on next page.)

Fig. 20 Photographs and CT scans of the pathological right humerus and the non-pathological left humerus of *Plateosaurus trossingensis* NMZ 1000001. **A** photograph of the right humerus in posterior view. Black lines indicate planes of the virtual cross-sections shown in **D** and **E**. **B** rendered surface model of the right humerus rendered transparent to show the internal medullary region (in orange). **C** CT cross-section in lateral view taken at approximately in the middle of the humerus in a lateromedial axis. The separation of cortical tissue and the central medullary region is indicated by white stippled lines. Note local thickening and irregular outline of the cortical bone. **D** CT cross section of the humerus roughly at midshaft length. Note that the oval-shape of the humeral shaft is only partly visible, grading into pathological tissue. **E** CT cross section of the humerus taken at a more proximal part of the humerus, where the bone is more heavily affected by the pathology. **F** photograph of the left humerus in posterior view. Black lines indicate planes of the virtual cross-sections shown in **K** and **L**. **G** rendered surface model of the left humerus in anterior view. Note that not the whole of the shaft area was scanned (area not scanned is indicated by white stippled lines). **H**, **I** CT sections of the distal condyles of the left humerus, showing the tissues at different heights (**H** is more anterior, **I** is more posterior). **J** CT section of the proximal head of the left humerus. **K** CT cross-section of the humerus at the height of the deltopectoral crest. **L** CT cross-section to the metaphyseal region, slightly proximal to the distal condyles. Note tapering cortices in the proximal and distal regions of the left humerus framing the interior cancellous bone of the medullary region. *ant* anterior, *co* cortical bone, *dist* distal, *dpc* deltopectoral crest, *hu* humerus, *lat* lateral, *med* medial, *mr* medullary region, *path* pathological tissue, *prox* proximal. Scale bars 50 mm (**A**, **F**). Images in **B**–**E** and **G**–**L** are not to scale

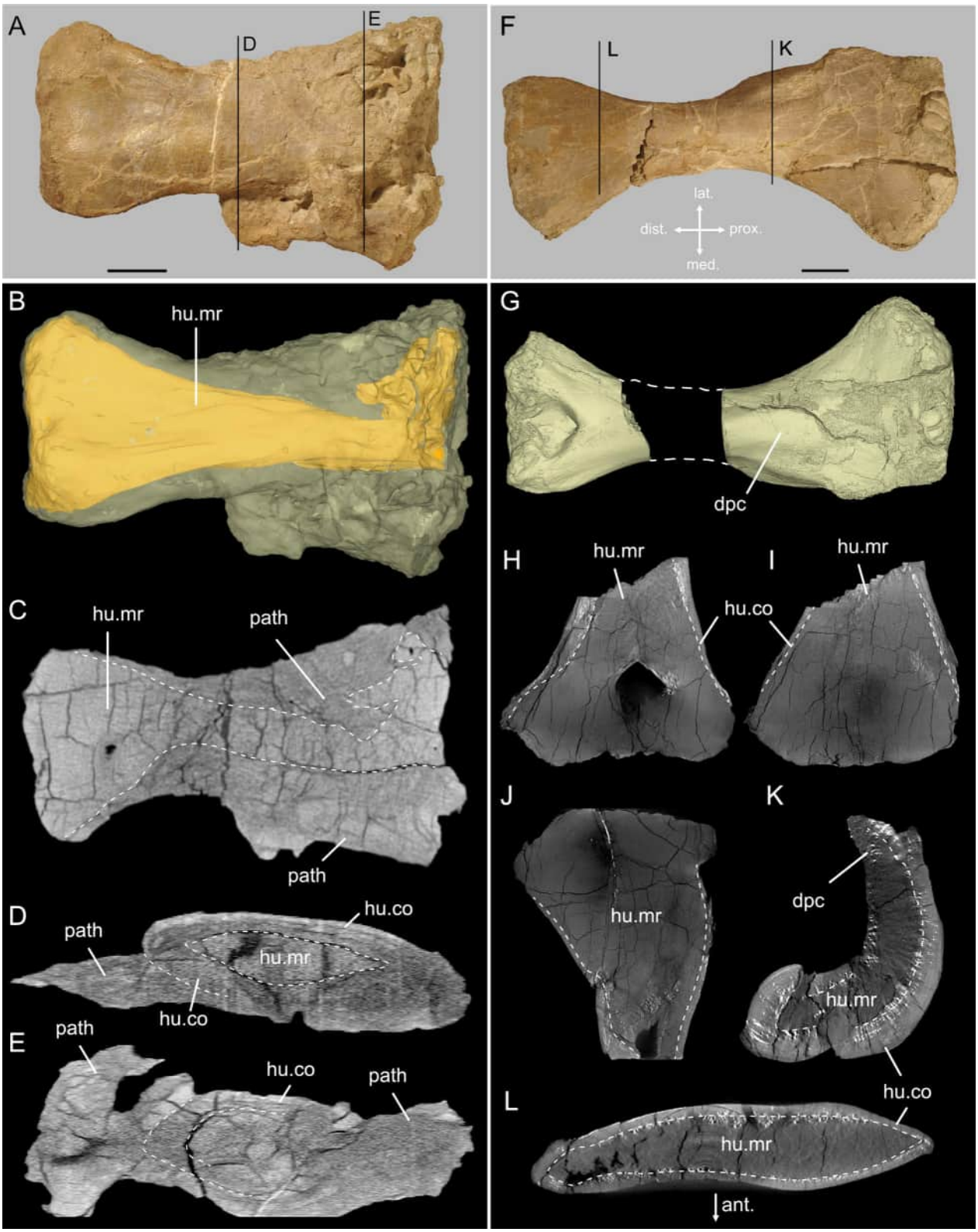

Fig. 20 (See legend on previous page.)

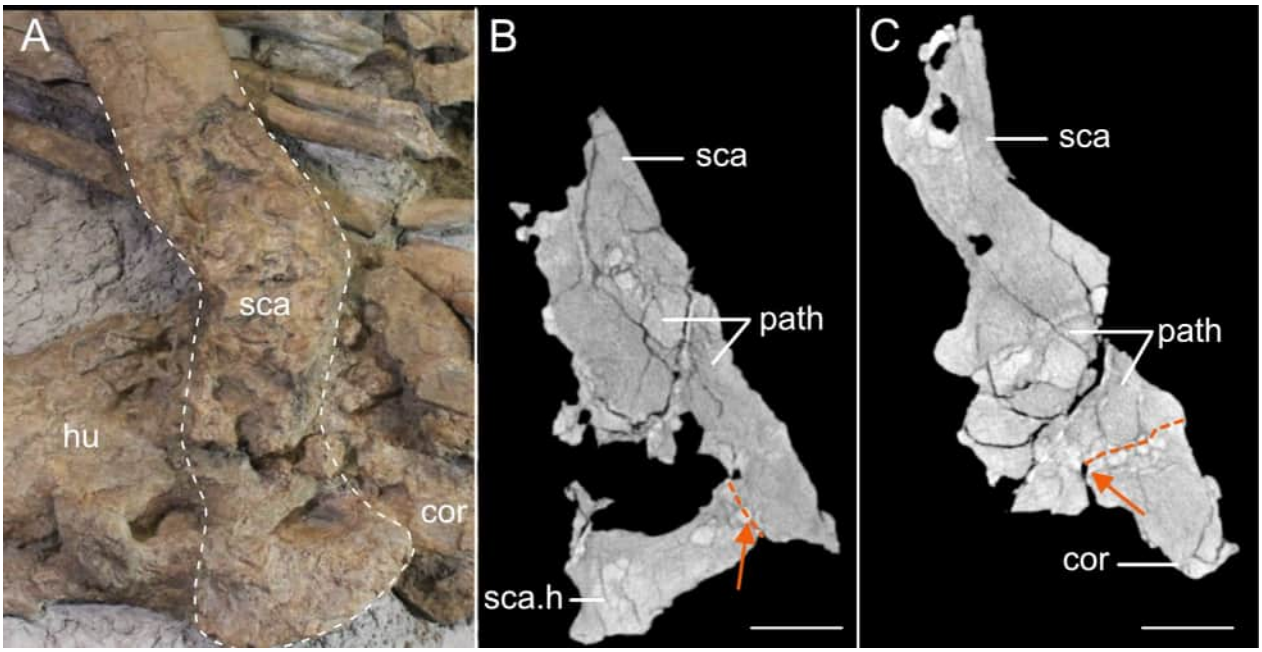

Fig. 21 Photograph and CT scans of pathological tissue in the proximal half of the right scapula and acetabular portion of the coracoid of *Plateosaurus trossingensis* NMZ 1000001. **A** Photograph of the pathological tissue of the scapula, humerus, and coracoid. The outline of the scapula is indicated by the white stippled line. **B** CT cross-section in lateral view taken at approximately in the middle of the structures along the lateromedial axis. **C** CT cross-section in lateral view taken close to the medial surfaces of the structures in a lateromedial axis. Orange stippled lines and arrows denote fusion between the scapula and coracoid. *cor* coracoid, *h* head, *hu* humerus, *path* pathological tissue, *sca* scapula. Scale bars 30 mm

Dorsal rib 10

The thin section of dorsal rib 10 is somewhat teardrop-shaped (Fig. 24), and derives from the proximal part of the rib, about 7 cm distal to the rib head. It measures a maximum of around 22 mm and 11 mm along the anteromedial-posterolateral and anterolateral-posteromedial axes, respectively. No obvious signs of compaction or missing portions can be seen apart from a crack in the anterior corner of the outer cortical bone.

In comparison with the dorsal rib 7, dorsal rib 10 has a centrally situated medullary cavity lined by endosteal lamellar bone. While there are fewer resorption cavities in the dorsal rib 10, the individual cavities are larger and located on the anterior side of the bone, resulting in greater amounts of endosteal lamellar bone in the perimedullary region (Fig. 24). Although the compact cortex is more uniformly distributed around the medullary cavity compared to dorsal rib 7, it is considerably thicker on the anteromedial and posteromedial sides.

The medial and anteromedial parts of the cortex consist of primary bone tissue (Fig. 24). The primary cortical tissue comprises a cyclically deposited woven-parallel complex similar to that seen in dorsal rib 7, characterised by abundant vascular canals especially in the inner- and mid-parts of the cortical bone. The bone matrix shows a fine fibrous structure and houses numerous primary osteons. Locally the primary osteon arrangement changes from predominantly longitudinal and radially arranged, to predominantly longitudinal but radially arranged, to weakly reticular anastomosing primary osteons (Fig. 24C–F). In the posterior parts of the section, the cortex is mostly remodelled into dense Haversian bone comprising several generations of secondary osteons.

Growth marks are visible throughout the non-remodelled parts of the cortex, identified as growth zones separated by LAGs. Occasionally, two LAGS in the deeper layers of the cortex are spaced very close together with no visible primary bone structures between them, forming a so-called double layer (Castanet, 1994; Castanet et al., 1993, 2004). Towards the outer bone surface an EFS is clearly discernible. The growth record of dorsal rib 10 comprises 22 LAGs. The distances between individual growth lines are markedly greater in the inner cortex and abruptly decrease in the EFS (Fig. 24C, D). The EFS contains 12 closely spaced LAGs in the outermost part of the cortex with no vascularisation in between. The bone tissue has a parallel-fibred matrix grading locally into lamellar bone.

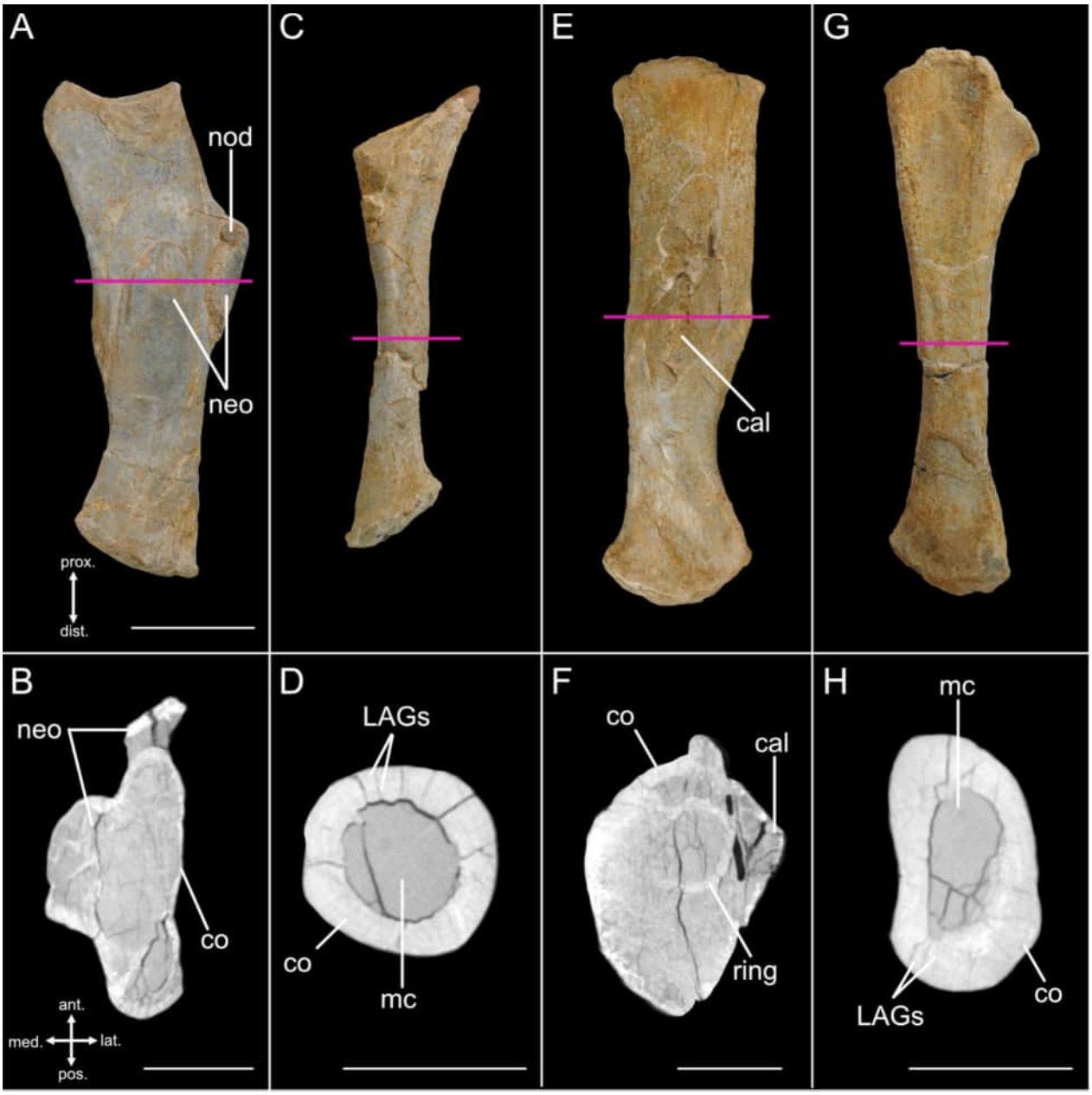

Fig. 22 Radii and ulnae, and CT cross-sections of these bones, of *Plateosaurus trossingensis* SMF 11.4. **A** left radius 11.4.144 in medial view and **B** cross-section of the radius at the mid-shaft with its location indicated by the pink line in A. **C** right radius 11.4 in medial view. **D** cross-section of the radius at the mid-shaft with its location indicated by the pink line in **C**. **E** left ulna 11.4.189 in lateral view. **F** cross-section of the ulna at the mid-shaft with its location indicated by the pink line in **E**. **G** right ulna 11.4 in lateral view. **H** cross-section of the ulna at the mid-shaft with its location indicated by the pink line in **F**. Same orientations for **B**, **D**, **F** and **H**. *ant* anterior, *cal* callus, *co* cortical bone, *dist* distal, *LAGs* lines of arrested growth, *lat* lateral, *med* medial, *mr* medullary region, *neo* potential neoplasm, *nod* bony nodule, *pos* posterior, *prox* proximal, *ring* internal ring of bone. Scale bars 50 mm (**A**, **C**, **E**, **G**) and 20 mm (**B**, **D**, **F**, **H**)

Sharpey's fibres grade into the external surface of the anterior and posterior sides. In contrast to dorsal rib 7, scattered secondary osteons observed in dorsal rib 10 are smaller and less frequent and found predominantly on the lateral half of the bone (Fig. 24).

Teoplati exhibit creation

The Teoplati exhibit has been the entrance piece to the NMZ UZH since September 2020. The exhibit comprises several parts: (i) the NMZ 1000001 skeleton (and casts of missing elements; Figs. 2 and 25) in the

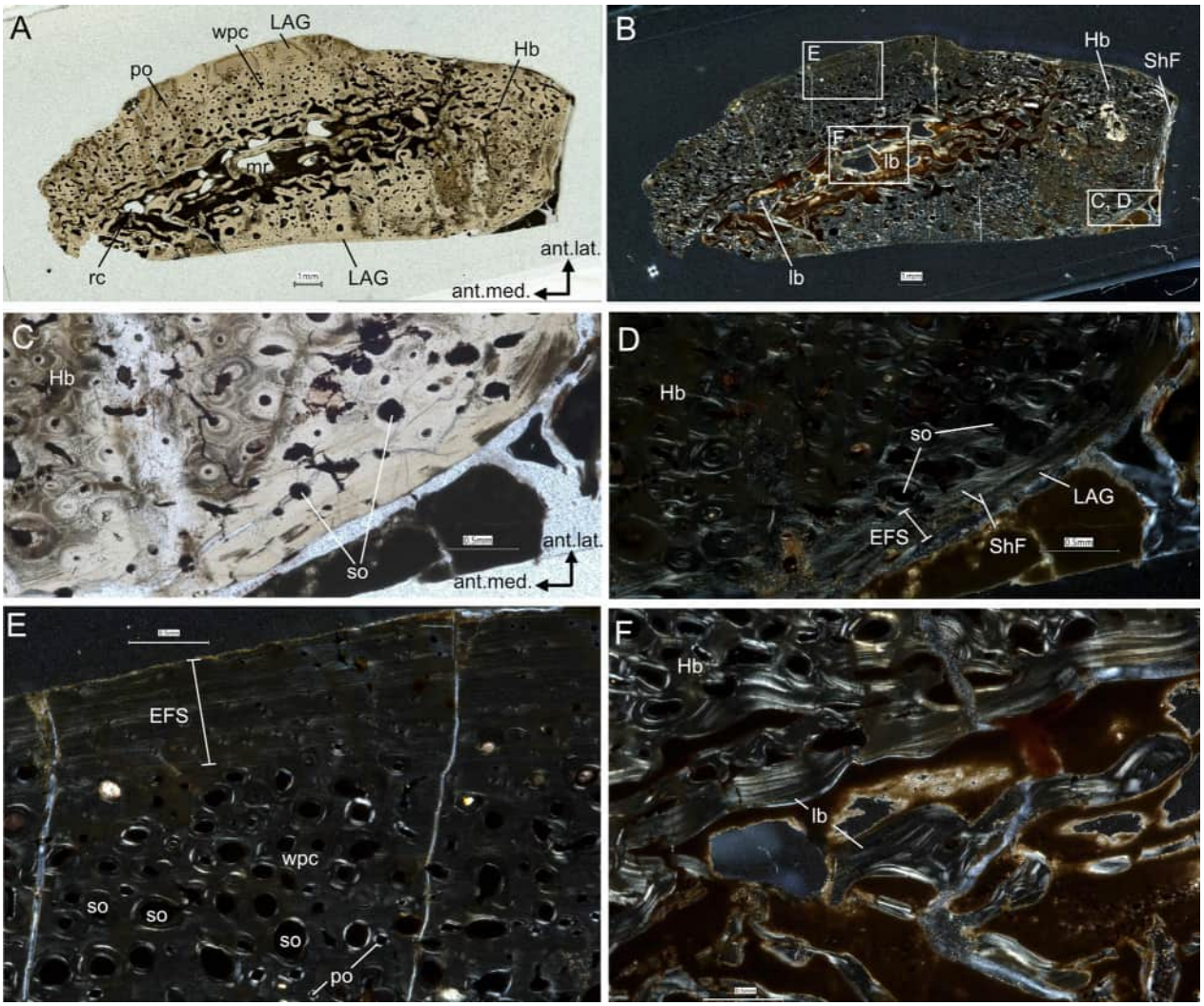

Fig. 23 Histology of dorsal rib 7 of *Plateosaurus trossingensis* NMZ 1000001. Images in **A** and **C** taken under normal polarized light, **B** and **D-F** under cross-polarized light. **A**, **B** whole cross-section of the midshaft of the rib. White squares denote close-ups shown in **D**–**F**. **C**, **D** heavily remodelled cortical bone. Note that primary tissue is preserved only close to the bone surface, although scattered secondary osteons are frequent. The external fundamental system is only partially visible here. **E** Cortex showing mainly primary bone, consisting of woven-parallel complex vascularised by longitudinally arranged primary osteons and scattered larger secondary osteons. Secondary osteons are missing in the surficial cortex so that the external fundamental system is better visible here. **F** Transition from medullary region showing endosteal lamellar bone to perimedullary region showing heavily remodelled Haversian bone tissue. *ant* anterior, *EFS* external fundamental system, *flb* fibrolamellar bone, *Hb* Haversian bone, *LAG* line of arrested growth, *lat* lateral, *lb* lamellar bone, *med* medial, *mr* medullary region, *po* primary osteon, *rc* resorption cavity, *ShF* Sharpey's fibres, *so* secondary osteon, *wpc* woven-parallel complex. Scale bars 1 mm (**A**, **B**) and 0.5 mm (**C**–**F**)

articulated pose as it was discovered, behind a glass barrier, (ii) a life-size reconstruction of *Plateosaurus trossingensis* based on NMZ 1000001 that measures 7.7 m from snout to tail and stands 4 m tall; (iii) a landscape diorama representing the Gruhalde palaeoenvironment with desiccated mud cracks and reconstructions of the giant horsetail *Equisetites arenaceus* (Fig. 25). Rather than a setup with a skeleton and generic model, it was deemed important to make the connection for the museum visitors between the original finding situation of the actual bones in the claypit Gruhalde in Frick, and the 3D life reconstruction as exhibited a) within its environment in a diorama and b) showing the peculiar pathological condition of the individual. The planning and co-ordination of the exhibit construction was overseen by DH in the NHM UZH, the skeletal mount constructed by BP and UB (Fig. S4), and the *Plateosaurus* life-size reconstruction, Gruhalde diorama, and glass barriers were undertaken by EH, SW, and RF from the company 10 Tons, with

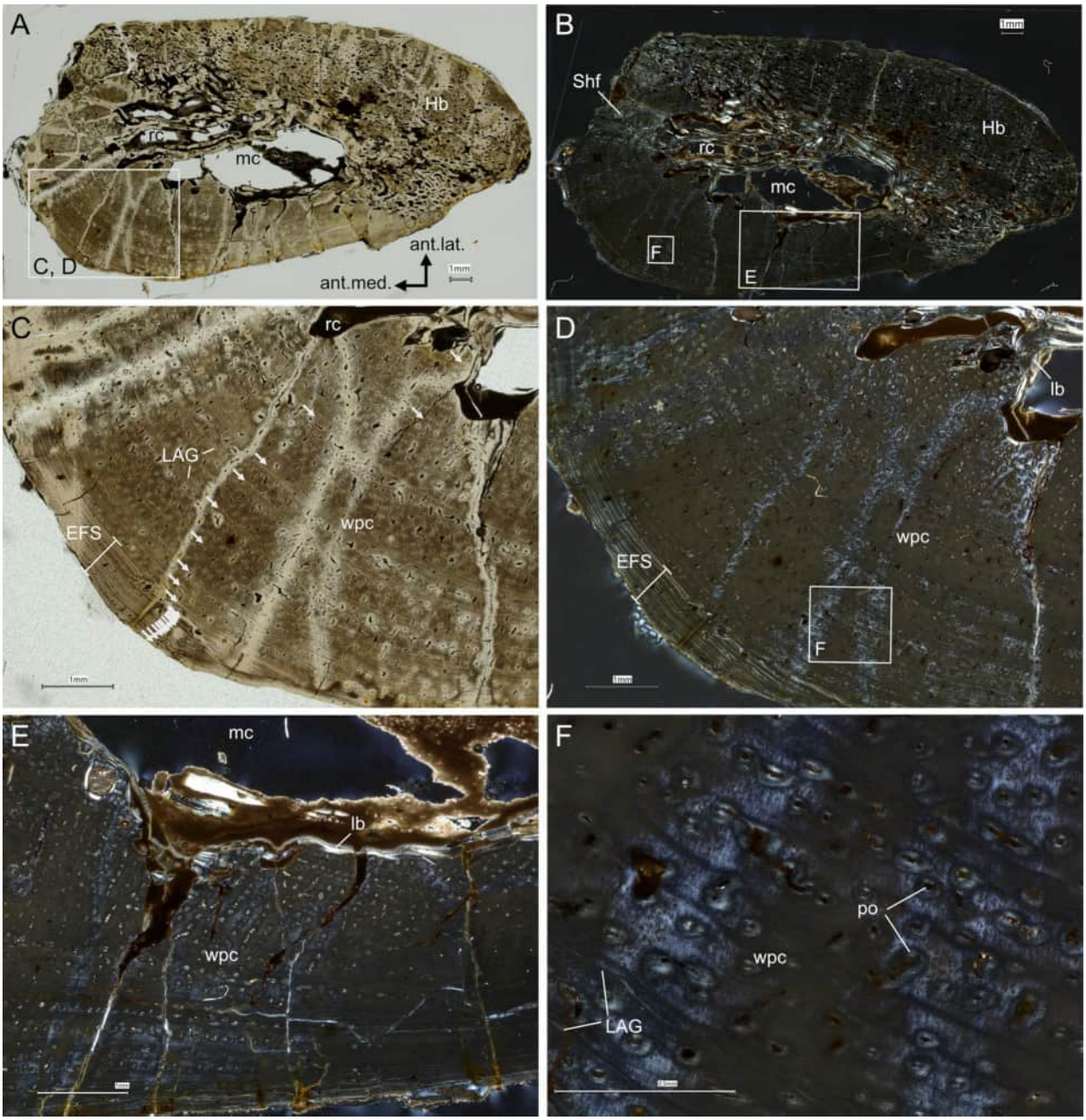

Fig. 24 Histology of dorsal rib 10 of *Plateosaurus trossingensis* NMZ 1000001. Images in **A** and **C** taken under normal polarized light, **B** and **D–F** under cross-polarized light. **A**, **B** Whole cross-section of the proximal portion of the rib. White squares denote close-ups shown in **C–F**. **C–F** Primary cortex of the rib consisting of woven-parallel-complex, vascularized by numerous primary osteons. Note that the orientation of the longitudinal primary osteons in the woven-parallel matrix changes locally from dominantly radial arrangement in the deeper cortex (**E**), to circumferential or weakly reticular (**C**, **D**, **F**). The medullary cavity and larger erosion cavities in the perimedullary region are delimited by endosteal lamellar bone. Growth marks in the form of lines of arrested growth (depicted by arrows in **C**) are seen throughout the cortex. Growth zones become increasingly thinner towards the external bone surface and an external fundamental system is developed in the most surficial part of the cortex. *ant* anterior, *EFS* external fundamental system, *Hb* Haversian bone, *LAG* line of arrested growth, *lat* lateral, *lb* lamellar bone, *med* medial, *mc* medullary cavity, *po*, primary osteon, *rc* resorption cavity, *ShF* Sharpey's fibres, *wpc* woven-parallel complex. Scale bars 1 mm (**A**–**E**) and 0.5 mm (**F**)

Fig. 25 The Teoplati exhibit at the Natural History Museum of the University of Zurich. **A** the full exhibit comprising the life-sized *Plateosaurus trossingensis* reconstruction in the foreground with the Gruhalde diorama comprising desiccated mud and the horsetail *Equisetites*, as well as the glass barrier enclosing the NMZ 1000001 skeleton in the background. **B** close-up of the NMZ 1000001 skeleton (see Fig. 2 for details) with the reconstruction and diorama in the background and **C** close-up of the right pectoral girdle and lower neck of the reconstruction showcasing the difference in colour and texture of the pathological tissue. Also note the speculative dorsal spines at the cervical-dorsal transition (see supplementary information). Photos by Stefanie Herter and reproduced here with permission

palaeoartist John Sibbick providing the initial sketches (Figs. 26 and S5). The reconstruction also included externally visible scar-tissue over part of the pathology on the right pectoral girdle and right upper forelimb to fully represent NMZ 1000001. Further information on the creation of the Teoplati exhibit can be found in the supplementary information.

Discussion

Body size and developmental plasticity of NMZ 1000001 and *Plateosaurus*

We infer that NMZ 1000001 was a skeletally mature adult when it died, based on the size of its long bones and the tightly spaced LAG distributions around the external areas of these sections (i.e., presence of an EFS; Chinsamy-Turan, 2005; Erickson, 2005). The estimated

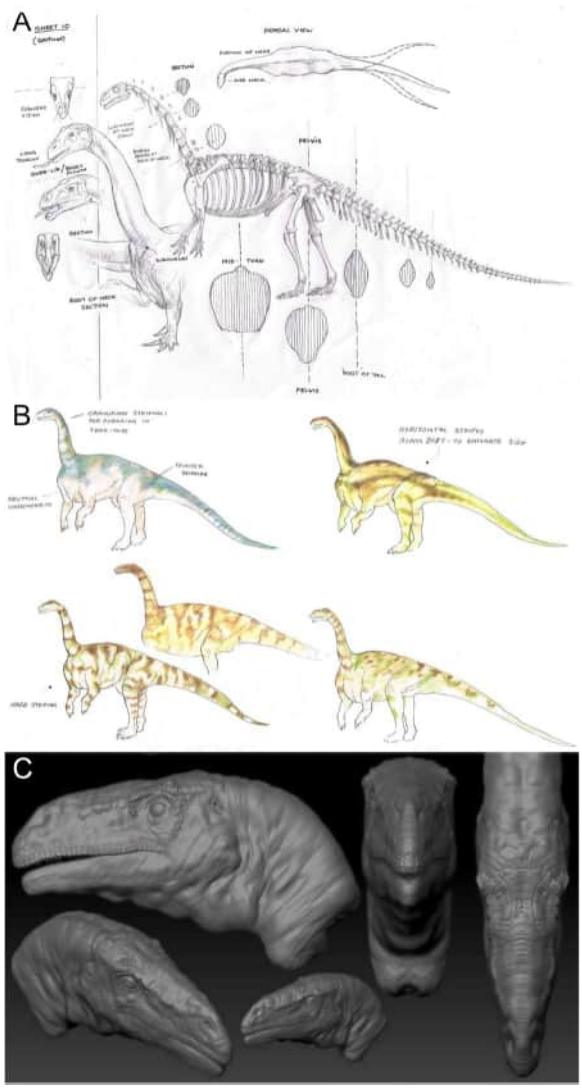

Fig. 26 Provisional sketches and models created as part of the early stages of the Teoplati exhibit construction. **A** Skeletal anatomy and provisional sketches of the *Plateosaurus trossingensis* model. **B** draft colour schemes and patterns for the Teoplati reconstruction (none were used in the final design) and **C** digital 3D model of the Teoplati skull in different perspectives. **A** and **B** drawn by John Sibbick and reproduced here with permission

body size of around 7.7 m is not only above average for adults of the species as a whole (6.7 m; Nau, 2022), but it also makes NMZ 1000001 one of the largest described individuals from Frick (Klein & Sander, 2007; Nau et al., 2020). The largest known individual from this locality is SMF 15.6 at an estimated 7.8 m long and the estimated lengths of most other specimens from Frick range between 4.8 m and 6.5 m (Klein & Sander, 2007; Nau, 2022). It is currently unclear why *Plateosaurus* adults from Frick are, on average, smaller than adults from Trossingen and Halberstadt (Klein & Sander, 2007), but the large sizes of NMZ 1000001 and SMF 15.6 relative to other Frick specimens indicates that size disparity between the Swiss and German localities may not be as large as previously thought.

A total of 22 LAGs were counted in the section of dorsal rib 10 of NMZ 1000001. Using the spacing between the innermost four preserved LAGS as a proxy for potentially even earlier growth cycles in the section, it is feasible to assume that two additional growth marks could have been lost due to remodelling and expansion of the medullary cavity in this rib. As such we can infer that the animal was 23 (without potential loss of growth marks) or, more likely, 25 years of age when it died.

Based on the LAG distribution, skeletal maturity was inferred to have been reached at around 13 years of age. This contrasts slightly with previous histological analyses of *Plateosaurus*, including specimens from Frick, that estimated this taxon attained skeletal maturity between 16 and 21 years of age (Klein & Sander, 2007; Sander & Klein, 2005), and is more consistent with growth curve models that hypothesised *Plateosaurus* attained skeletal maturity at younger ages (11–13 years old; Griebeler et al., 2013). We do not suggest one technique is more appropriate than another in estimating maturation ages but rather view the NMZ 1000001 LAG distribution as indicative of *Plateosaurus* developmental plasticity as has been previously proposed (Sander & Klein, 2005; Klein & Sander, 2007; Hofmann & Sander, 2014; Nau et al., 2020; 2022; Lallensack et al., 2021). We acknowledge further that the estimated maturation age of NMZ 1000001 based on a single rib that shows at least some bone remodelling and medullary cavity expansion should be treated with some caution when comparing to other studies that are, for example, based on long bones (Cerda et al., 2022; Klein & Sander, 2007; Sander & Klein, 2005).

Remarks on palaeopathologies and impact on lifestyle

The abnormal distal ends of the haemal arches of NMZ 1000001 caudal vertebrae 17–19 are very similar to pathologies observed in several individuals of *Plateosaurus* from Trossingen from similar areas of the tail (Schaeffer et al., 2024). Such pathologies have been inferred as tendon avulsions from tail-thrashing, for example to escape mud traps (Schaeffer et al., 2024). Whether the injury in NMZ 1000001 was caused shortly before its death or from a previous, successful escape is unknown. In the case of the latter, such an injury is inferred to have had minimal lasting impact on the animal's quality of life based on the relative abundance of tail-related injuries known from sauropodomorph skeletons (Butler et al., 2013; Cruzado-Caballero et al., 2023; Schaeffer et al., 2024).

The range of pathological tissues exhibited by the SMF 11.4 left radius and ulna strongly suggests this individual was suffering from multiple pathologies. For example, the external and internal morphology of the callus from the ulna is very similar to fracture calluses identified from the long bones and vertebrae of several distantly related dinosaur groups, including theropods and ornithopods (Baiano et al., 2024; Bertozzo et al., 2023, 2024; Rothschild & Panza, 2005). We therefore infer this callus as a healing response to a greenstick (partial) fracture, possibly resulting from a fall, with the size and thickness of the callus indicating the individual survived the incident (Bertozzo et al., 2023; Tanke & Rothschild, 2014). The slight lateromedial flattening of the ulna midshaft, and the expanded proximal region of the ulna, could both represent deformation due to the forelimb not being sufficiently immobilised during healing (Bertozzo et al., 2023, 2024). This would explain the large degree of distal curvature observed from the ulna as the bone underwent a malunion during healing (Bertozzo et al., 2023, 2024). An insufficiently immobilised limb could also in part explain the high degree of lateromedial flattening of the left radius as a response to experiencing different biomechanical loads during this period of physical instability. The expanded proximal region of the ulna could represent an alternative condition as its morphology is broadly reminiscent of a *Kentrosaurus* ulna with an expanded proximal region that was provisionally interpreted as possible hyperostosis (a non-inflammatory enthesitis; Cruzado-Caballero et al., 2023; Mallison, 2010b). However, it is often difficult to reliably distinguish between hyperostosis and spondyloarthropathy (aseptic inflammation of joints and articulations between bones) in the fossil record (Baiano et al., 2024; Cruzado-Caballero et al., 2023; Gutherz et al., 2020), which limits the robustness of this interpretation. The internal 'ring' structure within the ulna midshaft may represent the inner-most part of the original cortex of part of the lateral surface that broke away during the fracture and was quickly overgrown by the hypertrophied callus. Despite this possible malunion, there are no signs that the forelimb was infected and so likely did not actively contribute to the individual's death.

In contrast to the ulna, the external and internal morphologies of the infectious areas from the SMF 11.4 radius are most similar to neoplasms with the body nodule representing an aneurysmal bone cyst. Neoplasia is rare in the fossil record, relative to trauma and infection-related pathologies (Hamm et al., 2020), but is known from several dinosaur groups, including hadrosaurs, carnosaurs, stegosaurs and sauropods (de Souza Barbosa et al., 2016; Dumbravă et al., 2016; Gonzalez et al., 2017; Hao et al., 2018; Helbling et al., 2001; Rothschild et al., 1999, 2003). SMF 11.4 would thus represent one of the stratigraphically oldest instances of neoplasia in a dinosaur (see also Garcia et al., 2025). The large size of the neoplasms and the altered surface texture of the affected bone rules them out from being benign tumours such as osteomas or hemangioma (de Souza Barbosa et al., 2016; Gonzalez et al., 2017; Rothschild et al., 2003). The surface texture is also not typical of metastatic cancer (Rothschild et al., 1999). The cortical bone thinning around the neoplasms tentatively points towards some type of osteoblastic bone tumor (Gonzalez et al., 2017). While the exact origin of this neoplasia is unknown, the specimen nevertheless exhibits multiple pathologies within the same individual and showcases the potential for a higher diversity of palaeopathologies in the sauropodomorph fossil record than previously known.

Moving back to NMZ 1000001, determining the exact aetiology of the right scapula-humerus pathology is more difficult. For example, a failed predation attempt is difficult to confirm or deny due to no obvious predator-related damage such as tooth marks (e.g., Butler et al., 2013; Gutherz et al., 2020; Tanke & Rothschild, 2014), and to the lack of large predators (> 1.5 m long) from the Gruhalde Lower saurian layers (new discoveries notwithstanding; Sander, 1992; Zahner & Brinkmann, 2019). Evidence of impact trauma is also difficult to identify due to the uncertain absence of any fractures, both fresh or healed (e.g. Schaeffer et al., 2024; Straight et al., 2009; Tanke & Rothschild, 2014).

We therefore infer the NMZ 1000001 pathology as most likely the result of some form of disease. The rugose surface textures of the affected bones and the looser structures and lower densities of the internal tissues, relative to those of normal bones, are most indicative of osteomyelitis, an infection of the bone tissue (Annè et al., 2015; de Souza et al., 2014; Fitzgerald et al., 1976; Hamm et al., 2020; Lew & Waldvogel, 2004; Wick et al., 2014). We cannot fully rule out the possibility of septic arthritis, i.e., infection of the synovium around joints, since infected bones exhibit very similar morphologies to osteomyelitis-infected bones and the two conditions are often difficult to reliably tell apart in fossil specimens (Annè et al., 2016; Gutherz et al., 2020). Furthermore, the severity and large extent of the affected bones and the high degrees of possible fusion between affected bones all point towards a chronic infection (Annè et al., 2015; de Souza et al., 2014; Fitzgerald et al., 1976; Hamm et al., 2020; Lew & Waldvogel, 2004; Wick et al., 2014). Osteomyelitis has been reported from multiple dinosaur groups (Baiano et al., 2024; Bertozzo et al., 2023; Chinzorig et al., 2022; Cruzado-Caballero et al., 2021a, 2021b; Foth et al., 2015; Gutherz et al., 2020; Hamm

et al., 2020; Hanna, 2002; Hunt et al., 2019), including sauropodomorphs (Aureliano et al., 2021; Clayton, 2018; de Souza Barbosa et al., 2019; García et al., 2017; Xing et al., 2018), which all show similar pathologies as NMZ 1000001. However, in most cases infected areas are limited to a single bone, e.g., rib or long bone (Bertozzo et al., 2023; de Souza Barbosa et al., 2019; Xing et al., 2018), or a couple of adjacent bones (usually vertebrae), although some individuals exhibit multiple infections across the body (Aureliano et al., 2021; Foth et al., 2015; García et al., 2017; Hamm et al., 2020; Hanna, 2002; Peterson & Vittore, 2012). Given the lack of any other sites of infection or trauma on NMZ 1000001 (besides the ca 17–19 haemal arches), it is therefore likely that the right scapula was the original site of microbial infection and subsequently spread to the adjacent bones in this region of the body. Furthermore, the NMZ 1000001 infection also differs from previously described dinosaur cases in that the infected site in this *Plateosaurus* exhibits both sharp and gradual transitions between pathological and normal tissue. Osteomyelitis-infected sites in other dinosaurs exhibit either just sharp (Aureliano et al., 2021; Bertozzo et al., 2023), or gradual boundaries (Hamm et al., 2020) with no discernible reason for this pattern. The significance of these difference transitions in NMZ 1000001 is therefore unclear but further highlights the uniqueness of this specimen.

Confidently determining the origin(s) of the chronic infection in NMZ 1000001 is unlikely. Osteomyelitis cases in modern birds and reptiles commonly originate from exposure-induced bone trauma such as accident-related fractures (Raftery, 2011; Reavill, 2014; Rothschild & Panza, 2005). Similar origins are also hypothesised for osteomyelitis cases in several dinosaur specimens (e.g., Bertozzo et al., 2023; Chinzorig et al., 2022; Cruzado-Caballero et al., 2021b; Foth et al., 2015; Hanna, 2002), with other cases thought to have originated from trauma from failed predation attempts (Gutherz et al., 2020; Tanke & Rothschild, 2014; Xing et al., 2018) or intra-specific aggression (Arbour & Currie, 2011; Hamm et al., 2020). There is also one case of parasitic-induced osteomyelitis in a titanosaur sauropod (Aureliano et al., 2021). However, the extent of bone remodelling and fusion of elements in NMZ 1000001 prevents identification of fractures or bite-marks as possible origins of bacterial infection. The condition of the affected bones also prevents classification of the chronic osteomyelitis as primary or secondary, since the primary aetiology and duration needs to be known (Baltensperger et al., 2004; Bell & Coria, 2013; Cruzado-Caballero et al., 2021a; Eyrich et al., 2003). Nevertheless, it is reasonable to infer that NMZ 1000001 lived with the infection for a prolonged, albeit undeterminable, length of time before it died, given that much of the shape of the right humerus was severely affected by the pathology.

Understanding the precise impact(s) of chronic osteomyelitis on the quality of life of NMZ 1000001 is difficult, but reasonable inferences can be made based on the severity of the affected tissues. For example, the pathology did not have much impact on the individual's locomotory and foraging abilities given that the individual likely lived with the disease for an extended period of time (the same can also be argued for the SMF 11.4 pathology). This also directly lends further support to the hypothesis that adult *Plateosaurus* were bipedal (Mallison, 2010a, 2011; Reiss & Mallison, 2014). If the individual was obligatory or facultatively quadrupedal, then a pathology of this extent and severity would have had a more debilitating impact on locomotion (Bertozzo et al., 2023; Cruzado-Caballero et al., 2021a). In contrast, the pathology may have indirectly contributed to the individual's death as the reduced range of motion in the right forelimb perhaps hindered its ability to escape the mud hole in which it was trapped and ultimately preserved (Sander, 1992).

Conclusions

We provided an osteological description of a *Plateosaurus trossingensis* specimen from Frick that exhibits an above average estimated body length for the whole species and is one of the largest individuals described from the Swiss locality. In addition, we showed that NMZ 1000001 may have attained skeletal maturity at a younger age than previous histological-sectioned specimens indicated. This not only suggests greater developmental plasticity in *Plateosaurus* than previously thought, but further highlights the need for in-depth investigations on greater numbers of specimens to fully account for the morphological variation and developmental plasticity exhibited by this sauropodomorph. We inferred the distinctive pathology on the right scapula and humerus of NMZ 1000001 to be the result of a chronic case of osteomyelitis that is larger and more advanced than any previously described case from a dinosaur. Furthermore, we inferred the pathological tissues of SMF 11.4 as a combination of a callus from a greenstrick fracture with a possible malunion, neoplasms and an aneurysmal bone cyst. These specimens increase the known diversity and severity of diseases and afflictions experienced in sauropodomorphs and also represent one of the stratigraphically earliest known occurrences of osteomyelitis and neoplasia in dinosaurs.

Abbreviations

NMZ UZH Natural History Museum of the University of Zurich, Zurich, Switzerland
SMA Sauriermuseum Aathal, Aathal, Switzerland

SMF Sauriermuseum Frick, Frick, Switzerland

Supplementary Information

The online version contains supplementary material available at https://doi.org/10.1186/s13358-025-00368-3.

Supplementary material 1.

Acknowledgements
We thank the entire team at the SMF and the Saurierkommission Frick for excavating the specimen, for facilitating access to the specimen for study, and for the permanent loan of the specimen to the NHM UZH. The Swiss Federal Laboratories for Materials Science and Technology (Empa) is thanked for providing access to CT scanning facilities. Thanks to Stefanie Herter (Department of Paleontology, UZH) for photography of SMF 11.4 and the Teoplati exhibit and for discussions on palaeopathology. We thank the editors and Darius Nau, Joep Schaeffer and an anonymous reviewer for their helpful comments that much improved the manuscript.

Author contributions
TMS and DMH conceived the study. SFJD wrote the initial draft and prepared figures as part of her MSc thesis, supervised by TMS. JB, TMS and DMH revised the draft. JB formatted and amended the draft and prepared additional figures. DMH, EH, SW, and RF provided data, text and images on the production process of the Teoplati exhibit. RZ and KT scanned specimens and provided data and information on scanning procedure. UB and BP led excavation, prepared the specimen, and provided data and images on the Teoplati exhibit and on the geological context. All co-authors read and approved the final version.

Funding
JB was funded by an SNSF Swiss Postdoctoral Fellowship (TMPFP2_217001).

Availability of data and materials
The 3D CT datasets of the right pectoral girdle and upper forelimb are available on Morphosource [https://www.morphosource.org; project ID: 000715009].

Declarations

Ethics approval and consent to participate
Not applicable.

Competing interests
The authors declare no competing interests.

Author details
[1]Department of Paleontology, University of Zurich, Karl-Schmid-Strasse 4, 8006 Zurich, Switzerland. [2]Natural History Museum, University of Zurich, Karl-Schmid-Strasse 4, 8006 Zurich, Switzerland. [3]10 Tons, Otto Busses Vej 31, 2450 Copenhagen, Denmark. [4]Swiss Federal Laboratories for Materials Science and Technology (EMPA), Center for X-Ray Analytics, Ueberlandstrasse 129, 8600 Dübendorf, Switzerland. [5]ARTORG Center, University of Bern, Freiburgstrasse 3, 3010 Bern, Switzerland. [6]Department of Chemistry, University of Fribourg, 1700 Fribourg, Switzerland. [7]Sauriermuseum Frick, Schulstrasse 22, 5070 Frick, Switzerland. [8]Sauriermuseum Aathal, Zürichstrasse 69, 8607 Aathal-Seegräben, Switzerland.

Received: 16 December 2024 Accepted: 23 April 2025
Published online: 11 June 2025

References

Annè, J., Garwood, R. J., Lowe, T., Withers, P. J., & Manning, P. L. (2015). Interpreting pathologies in extant and extinct archosaurs using micro-CT. *PeerJ, 3*, e1130. https://doi.org/10.7717/peerj.1130

Annè, J., Hendrick, B. P., & Schein, J. P. (2016). First diagnosis of septic arthritis in a dinosaur. *Royal Society Open Science, 3*, 160222. https://doi.org/10.1098/rsos.160222

Arbour, V. M., & Currie, P. J. (2011). Tail and pelvis pathologies of ankylosaurian dinosaurs. *Historical Biology, 23*(4), 375–390. https://doi.org/10.1080/08912963.2011.563849

Aureliano, T., Nascimento, C. S. I., Fernandes, M. A., Ricardi-Branco, F., & Ghilardi, A. M. (2021). Blood parasites and acute osteomyelitis in a non-avian dinosaur (Sauropoda, Titanosauria) from the Upper Cretaceous Adamantina Formation, Bauru Basin, Southeast Brazil. *Cretaceous Research, 118*, 104672. https://doi.org/10.1016/j.cretres.2020.104672

Baiano, M. A., Cerda, I. A., Bertozzo, F., & Pol, D. (2024). New information on paleopathologies in non-avian theropod dinosaurs: a case study on South American abelisaurids. *BMC Ecology and Evolution, 24*, 6. https://doi.org/10.1186/s12862-023-02187-x

Baltensperger, M. M., Grätz, K., Bruder, E., Lebeda, R., Malek, M., & Eyrich, G. (2004). Is primary chronic osteomyelitis a uniform disease? Proposal of a classification based on a retrospective analysis of patients treated in the past 30 years. *Journal of Cranio-Maxillofacial Surgery, 32*(1), 43–50. https://doi.org/10.1016/j.jcms.2003.07.008

Bell, P. R., & Coria, R. A. (2013). Paleopathological survey of a population of *Mapusaurus* (Theropoda: Carcharodontosauridae) from the Late Cretaceous Hunicul Formation Argentina. *PLoS ONE, 8*(5), e63409. https://doi.org/10.1371/journal.pone.0063409

Bertozzo, F., Bolotsky, I., Bolotsky, Y. L., Poberezhskiy, A., Ruffell, A., Godefroit, P., & Murphy, E. (2023). A pathological ulna of *Amurosaurus riabinini* from the upper cretaceous of far eastern Russia. *Historical Biology, 35*(2), 268–275. https://doi.org/10.1080/08912963.2022.2034805

Bertozzo, F., Stein, K., Varotto, E., Galassi, F. M., Ruffell, A., & Murphy, E. (2024). Histological analysis and etiology of a pathological iguanodontian femur from England. *Journal of Anatomy, 245*, 490–500. https://doi.org/10.1111/joa.14053

de Buffrénil, V., de Ricqlès, A., Zylberberg, L., Padian, K., Laurin, M., & Quilhac, A. (2021). *Vertebrate skeletal histology and paleohistology*. CRC Press.

de Buffrénil, V., & Quilhac, A. (2021). Bone tissue types: a brief account of currently used categories. In V. de Buffrénil, A. de Ricqlès, L. Zylberberg, K. Padian, M. Laurin, & A. Quilhac (Eds.), *Vertebrate Skeletal Histology and Paleohistology* (pp. 147–182). CRC Press.

Butler, R. J., Yates, A. M., Rauhut, O. W. M., & Foth, C. (2013). A pathological tail in a basal sauropodomoprh dinosaur from South Africa: evidence of traumatic amputation? *Journal of Vertebrate Paleontology, 33*(1), 224–228. https://doi.org/10.1080/02724634.2012.710691

Castanet, J. (1994). Age estimation and longevity in reptiles. *Gerontology, 40*(2–4), 174–192. https://doi.org/10.1159/000213586

Castanet, J., Croci, S., Aujard, F., Perret, M., Cubo, J., & De Margerie, E. (2004). Lines of arrested growth in bone and age estimation in a small primate: *Microcebus murinus*. *Journal of Zoology, 263*(1), 31–39. https://doi.org/10.1017/S0952836904004844

Castanet, J., Francillon-Vieillot, H., Meunier, F. J., & de Ricqlès, A. (1993). Bone and individual aging. In: Hall, B. K. (Ed.) *Bone Growth-B.*

Cerda, I. A., Pol, D., Otero, A., & Chinsamy, A. (2022). Palaeobiology of the early sauropodomorph *Mussaurus patagonicus* inferred from its long bone histology. *Palaeontology, 65*(4), e12614. https://doi.org/10.1111/pala.12614

Chinsamy-Turan, A. (2005). *The microstructure of dinosaur bone*. Maryland, Johns Hopkins University Press.

Chinzorig, T., Beguesse, K. A., Canoville, A., Phillips, G., & Zanno, L. E. (2022). Chronic fracture and osetomyelitis in a large-bodied ornithomimosaur with implications for the identification of unusual endosteal bone in the fossil record. *The Anatomical Record, 306*(7), 1864–1879. https://doi.org/10.1002/ar.25069

Clayton, R. J. (2018). Description of unusual pathological disorders on pubes and associated left femur from a *Diplodocus* specimen. *Paludicola, 11*, 179–187.

Cruzado-Caballero, P., Díaz-Martínez, I., Rothschild, B., Bedell, M., & Pereda-Suberbiola, X. (2021a). A limping dinosaur in the Late Jurassic: pathologies in the pes of the neornithischian *Othnielosaurus consors* from

the Morrison Formation (Upper Jurassic, USA). *Historical Biology, 33*(9), 1753–1759. https://doi.org/10.1080/08912963.2020.1734589
Cruzado-Caballero, P., Lecuona, A., Cerda, I., & Díaz-Martínez, I. (2021b). Osseous paleopathologies of *Bonapartesaurus rionegrensis* (Ornithopoda, Hadrosauridae) from allen formation (Upper Cretaceous) of patagonia argentina. *Cretaceous Research, 124*, 104800. https://doi.org/10.1016/j.cretres.2021.104800
Cruzado-Caballero, P., Sebasti, L., & Gonz, J. (2023). How common are lesions on the tails of sauropods? Two new pathologies in titanosaurs from the Late Cretaceous of Argentine Patagonia. *Diversity, 15*(3), 464. https://doi.org/10.3390/d15030464
Dumbravă, M. D., Rothschild, B. M., Weishampel, D. B., Csiki-Sava, Z., Andrei, R. A., Acheson, K. A., & Codrea, V. A. (2016). A dinosaurian facial deformity and the first occurrence of ameloblastoma in the fossil record. *Scientific Reports, 6*, 29271. https://doi.org/10.1038/srep29271
Erickson, G. M. (2005). Assessing dinosaur growth patterns: a microscopic revolution. *Trends in Ecology & Evolution, 20*(12), 677–684. https://doi.org/10.1016/j.tree.2005.08.012
Eyrich, G. K. H., Baltensperger, M. M., Bruder, E., & Graetz, K. W. (2003). Primary chronic osteomyelitis in childhood and adolesence: a retrospective analysis of 11 cases of the literature. *Journal of Oral and Maxillofacial Surgery, 61*(5), 561–573. https://doi.org/10.1053/joms.2003.50110
Fitzgerald, R. H., Brewer, N. S., & Dahlin, D. C. (1976). Squamous-cell carcinoma complicating chronic osteomyelitis. *The Journal of Bone & Joint Surgery, 58*(8), 1146–1148.
Foth, C., Evers, S. W., Pabst, B., Mateus, O., Flisch, A., Patthey, M., & Rauhut, O. W. M. (2015). New insights into the lifestyle of *Allosaurus* (Dinosauria: Theropoda) based on another specimen with multiple pathologies. *PeerJ, 3*, e940. https://doi.org/10.7717/peerj.940
Fraas, E. (1913). Die neuesten Dinosaurierfunde in der schwäbischen Trias. *Naturwissenschaften, 45*, 1097–1100.
Galton, P. M. (2012). Case 3560 *Plateosaurus engelhardti* Meyer, 1837 (Dinosauria, Sauropodomorpha): proposed replacement of unidentifiable name-bearing type by a neotype. *The Bulletin of Zoological Nomenclature, 69*(3), 203–212. https://doi.org/10.21805/bzn.v69i3.a15
Galton, P. M. (2013). Comment on *Plateosaurus* Meyer, 1837 (Dinosauria, Sauropodomorpha): Proposed replacement of unidentifiable name-bearing type by a neotype (Case 3560; see BZN 69: 203–212, 295–296; 70: 120–121). *The Bulletin of Zoological Nomenclature, 70*(3), 205–206.
Galton, P. M., & Kermack, D. (2010). The anatomy of *Pantydraco caducus*, a very basal sauropodomorph dinosaur from the Rhaetian (Upper Triassic) of South Wales. *UK. Revue De Paléobiologie, 29*(2), 341–404.
Garcia, M. S., Martínez, R. N., & Müller, R. T. (2025). Craniofacial lesions in the earliest predatory dinosaurs indicate intraspecific agonistic behaviour at the dawn of the dinosaur era. *The Science of Nature, 112*, 30. https://doi.org/10.1007/s00114-025-01978-0
García, R. A., Cerda, I. A., Heller, M., Rothschild, B. M., & Zurriaguz, V. (2017). The first evidence of osteomyelitis in a sauropod dinosaur. *Lethaia, 50*, 227–236. https://doi.org/10.1111/let.12189
Gonzalez, R., Gallina, P. A., & Cerda, I. A. (2017). Multiple paleopathologies in the dinosaur *Bonitasaura salgadoi* (Sauropoda: Titanosauria) from the Upper Cretaceous of Patagonia, Argentina. *Cretaceous Research, 79*, 159–170. https://doi.org/10.1016/jcretres.2017.07.013
Griebler, E.-M., Klein, N., & Sander, P. M. (2013). Aging, maturation and growth of sauropodomorph dinosaurs as deduced from growth curves using long bone histological data: An assessment of methodological constraints and solutions. *PLoS ONE, 8*(6), e67012. https://doi.org/10.1371/journal.pone.0067012
Gutherz, S. B., Groenke, J. R., Sertich, J. J. W., Burch, S. H., & O'Connor, P. M. (2020). Paleopathology in a nearly complete skeleton of *Majungasaurus crenatissimus* (Theropoda: Abelisauridae). *Cretaceous Research, 115*, 104553. https://doi.org/10.1016/j.cretres.2020.104553
Hamm, C. A., Hampe, O., Schwarz, D., Witzmann, F., Makovicky, P. J., Brochu, C. A., Reiter, R., & Asbach, P. (2020). A comprehensive diagnostic approach combining phylogenetic disease bracketing and CT imaging reveals osteomyelitis in a *Tyrannosaurus rex*. *Scientific Reports, 10*, 18897. https://doi.org/10.1038/s41598-020-75731-0
Hanna, R. (2002). Multiple injury and infection in a sub-adult theropod dinosaur *Allosaurus fragilis* with comparisons to allosaur Allosaurus pathology in the Cleveland-Lloyd dinosaur quarry collection. *Journal of Vertebrate Paleontology, 22*(1), 76–90. https://doi.org/10.1671/0272-4634(2002)022[0076:MIAIIA]2.0.CO;2
Hao, B.-Q., Ye, Y., Maidment, S. C. R., Bertazzo, S., Peng, G.-Z., & You, H.-L. (2018). Femoral osteopathy in *Gigantspinosaurus sichuanensis* (Dinosauria: Stegosauria) from the Late Jurassic of Sichuan Basin, *southwestern China. Historical Biology, 32*(8), 1028–1035. https://doi.org/10.1080/08912963.2018.1561673
Helbling, M. I., II., Rothschild, B. M., & Tanke, D. H. (2001). Mesozoic neoplasia: a family affair. *Journal of Vertebrate Paleontology, 21*, 60A.
Hofmann, R., & Sander, P. M. (2014). The first juvenile specimens of *Plateosaurus engelhardti* from Frick, Switzerland: isolated neural arches and their implications for developmental plasticity in a basal sauropodomorph. *PeerJ, 2*, e458. https://doi.org/10.7717/peerj.458
Huene, F. V. (1907). Die Dinosaurier der europäischen Triasformation mit Berücksichtigung der aussereuopäischen Vorkommnisse. *Geologische und Palaeontologische Abhandlungen, 1*, 1–419.
Huene, F. V. (1926). Vollständige osteologie eines Plateosauriden aus dem schwäbischen Keuper. *Geologische und Palaeontologische Abhandlungen, 15*, 139–179.
Huene, F. V. (1928). Lebensbild des Saurischer-Vorkommens im obersten Keuper von Trossingen in Württemburg. *Palaeobiologica, 1*, 103–116.
Hunt, T. C., Peterson, J. E., Frederickson, J. A., Cohen, J. E., & Berry, J. L. (2019). First documented pathologies in *Tenontosaurus tilletti* with comments on infection in non-avian dinosaurs. *Scientific Reports, 9*, 8705. https://doi.org/10.1038/s41598-019-45101-6
International Code of Zoological Nomenclature. (2019). Opinion 2435 (Case 3560) – *Plateosaurus* Meyer, 1837 (Dinosauria, Sauropodomorpha): new type species designated. *The Bulletin of Zoological Nomenclature, 76*, 144.
Jaekel, O. (1914). Über die Wirbeltierfunde der oberen Trias von Halberstadt. *Paläeontologische Zeitschrift, 1*, 155–215.
Jordan, P., Pietsch, J. S., Bläsi, H., Furrer, H., Kündig, N., Looser, N., & Deplazes, G. (2016). The Middle to Late Triassic Bänkerjoch and Klettgau Formations of northern Switzerland. *Swiss Journal of Geosciences, 109*, 257–284. https://doi.org/10.1007/s00015-016-0218-3
Klein, N., & Sander, P. M. (2007). Bone histology and growth of the prosauropod dinosaur *Plateosaurus engelhardti* von Meyer, 1837 from the Norian bonbeds of Trossingen (Germany) and Frick (Switzerland). *Special Papers in Palaeontology, 77*, 169–206.
Lallensack, J. N., Teschner, E. M., Pabst, B., & Sander, P. M. (2021). New skulls of the basal sauropodomorph *Plateosaurus trossingensis* from Frick, Switzerland: is there more than one species? *Acta Palaeontologica Polonica, 66*(1), 1–28. https://doi.org/10.4202/app.00804.2020
Lefebvre, R., Allain, R., Houssaye, A., & Cornette, R. (2020). Disentangling biological variability and taphonomy: shape analysis of the long limb dinosaur *Plateosaurus*. *PeerJ, 8*, e9359. https://doi.org/10.7717/peerj.9359
Lew, D. P., & Waldvogel, F. A. (2004). Osteomyelitis. *Lancet, 364*(9431), 369–379. https://doi.org/10.1016/S0140-6736(04)16727-5
Mallison, H. (2010a). The digital *Plateosaurus* I: body mass, mass distribution and posture assess using CAD and CAE on a digitally mounted complete skeleton. *Palaeontologia Electronica, 13*(2), 8A.
Mallison, H. (2010b). The digital *Plateosaurus* II: an assessment of the range of motion of the limbs and vertebral column and of previous reconstructions using a digital skeletal mount. *Acta Palaeontologica Polonica, 55*(3), 433–458. https://doi.org/10.4202/app.2009.0075
Mallison, H. (2011). *Plateosaurus* in 3D: how CAD models and kinetic-dynamic modeling bring an extinct animal to life. In K. Klein, K. Remes, C. T. Gee, & P. M. Sander (Eds.), *Biology of the Sauropod Dinosaurs: Understanding the Life of Giants* (pp. 219–236). Indiana University Press.
Meyer, H. V. (1837). Mitteilungen, an professor Bronn gerichet (*Plateosaurus engelhardti*). *Neues Jahrbuch Für Geologie und Paläontologie, 1837*, 817.
Moser, M. (2003). *Plateosaurus engelhardti* Meyer, 1837 (Dinosauria: Sauropodomorpha) aus den Feuerletten (Mittelkeuper; Obertrias) von Bayern. *Zitteliana, 24*, 1–188.
Mujal, E., Schaeffer, J., Bath Enright, O. G., Cooper, S. L. A., Neipp, V. & Schoch, R. R. (2024). The Upper Triassic dinosaur beds of Trossingen, Germany: taphonomy of a mega-scale fossil Lagerstätte. *Palaeontological Association Annual Meeting*. Erlangen, Germany.
Nau, D. (2022). *Osteology of a large skeleton of Plateosaurus trossingensis from Frick (CH)*. University of Bonn.
Nau, D., Lallensack, J. N., Bachmann, U., & Sander, P. M. (2020). Postcranial osteology of the first early-stage juvenile skeleton of *Plateosaurus*

trossingnesis from the Norian of Frick, Switzerland. *Acta Palaeontologica Polonica, 65*(4), 679–708. https://doi.org/10.4202/app.00757.2020
Peterson, J. E., & Vittore, C. P. (2012). Cranial pathologies in a specimen of *Pachycephalosaurus*. *PLoS ONE, 7*(4), e36227. https://doi.org/10.1371/journal.pone.0036227
Ponton, F., Elzanowski, A., Castanet, J., Chinsamy, A., de Margerie, E., de Ricqlès, A., & Cubo, J. (2004). Variation of the outer circumferential layer in the limb bones of birds. *Acta Ornithologica, 39*(2), 137–140. https://doi.org/10.3161/068.039.0210
Raftery, A. (2011). Reptile orthopedic medicine and surgery. *Journal of Exotic Pet Medicine, 20*(2), 107–116. https://doi.org/10.1053/j.jepm.2011.02.005
Reavill, D. R. (2014). Review of musculoskeletal pathology in reptiles. *Proceedings Association of Reptiles and Amphibian Veterinarians, 2*, 86–96.
Regalado Fernández, O. R., Stöhr, H., Kästle, B., & Werneburg, I. (2023). Diversity and taxonomy of the Late Triassic sauropodomorphs (Saurischia, Sauropodomorpha) stored in the Palaeontological Collection of Tübingen, Germany, historically referred to *Plateosaurus*. *European Journal of Taxonomy, 913*, 1–88. https://doi.org/10.5852/ejt.2023.913.2375
Reiss, S., & Mallison, H. (2014). Motion range of the manus of *Plateosaurus engelhardti* von Meyer, 1837. *Palaeontologia Electronica, 17*(1), 12A.
Rothschild, B. M., & Panza, R. K. (2005). Epidemiologic assessment of trauma-independent skeletal pathology in non-passerine birds from museum collections. *Avian Pathology, 34*(3), 212–219.
Rothschild, B. M., & Storrs, G. W. (2003). Decompression syndrome in plesiosaurs (Sauropterygia: Reptilia). *Journal of Vertebrate Paleontology, 23*(2), 324–328.
Rothschild, B. M., Tanke, D. H., & Martin, L. D. (2003). Epidemiologic study of tumors in dinosaurs. *Naturwissenschaften, 90*(11), 495–500. https://doi.org/10.1007/s00114-003-0473-9
Rothschild, B. M., Witzke, B. J., & Hershkovitz, I. (1999). Metastatic cancer in the Jurassic. *The Lancet, 354*(9176), 398. https://doi.org/10.1016/S0140-6736(99)01019-3
Sander, P. M. (1992). The Norian *Plateosaurus* bonebeds of central Europe and their taphonomy. *Palaeogeography, Palaeoclimatology, Palaeoecology, 93*(3–4), 255–299. https://doi.org/10.1016/0031-0182(92)90100-J
Sander, P. M., & Klein, N. (2005). Developmental plasticity in the life history of a prosauropod dinosaur. *Science, 310*(5755), 1800–1802. https://doi.org/10.1126/science.1120125
Schaeffer, J. (2024). Osteological redescription of the holotype of *Plateosaurus trossingensis* (Dinosauria: Sauropodomorpha) from the Upper Triassic of SW Germany and its phylogenetic implications. *Journal of Systematic Palaeontology, 22*(1), 2335387. https://doi.org/10.1080/14772019.2024.2335387
Schaeffer, J., Mujal, E., & Schoch, R. R. (2023). *Reappraisal of the environmental seting and taphonomy of the Trossingen Plateosaurus bonebeds . German Geological Society—Geological Association Annual Meeting.* Berlin, Germany
Schaeffer, J., Wolff, E., Witzmann, F., Ferreira, G. S., Schoch, R. R., & Mujal, E. (2024). Paleobiological implications of chevron pathology in the sauropodomorph *Plateosaurus trossingensis* from the Upper Triassic of SW Germany. *PLoS ONE, 19*(7), e0306819. https://doi.org/10.1371/journal.pone.0306819
Schoch, R. R. (2011). Tracing Seemann's dinosaur excavation in the Upper Triassic of Trossingen: his field notes and the present status of the material. *Palaeodiversity, 4*, 245–282.
Schoch, R. R., & Seegis, D. (2014). Taphonomy, deposition and pedogenesis in the Upper Triassic dinosaur beds of Trossingen. *Palaeobiodiversity and Palaeoenvironments, 94*, 571–593. https://doi.org/10.1007/s12549-014-0166-8
Seemann, R. (1933). Das Saurischierlager in den Keupermergeln bei Trossingen. *Jahreshefte des Vereins Für Vaterländische Naturkunde in Württemberg, 89*, 129–160.
de Souza Barbosa, F. H., da Silva Marinho, T., Iori, F. V., & Paschoa, L. S. (2019). A case of infection in an Aeolosaurini (Sauropoda) dinosaur from the Upper Cretaceous of São Paulo, southeastern Brazil, and the impact on its life. *Cretaceous Research, 96*, 1–5. https://doi.org/10.1016/j.cretres.2018.12.004
de Souza Barbosa, F. H., Pereira, P. V. L. G. C., Bergqvis, L. P., & Rothschild, B. M. (2016). Multiple neoplasms in a single sauropod dinosaur from the Upper Cretaceous of Brazil. *Cretaceous Research, 62*, 13–17. https://doi.org/10.1016/j.cretres.2016.01.010
de Souza, S. O., Casagrande, R. A., Guerra, P. R., Cruz, C. E. F., Veit, E., Cardosa, M. R. I., & Driemeier, D. (2014). Osteomyelitis caused by *Salmonella enterica* serowar derby in boa constrictor. *Journal of Zoo and Wildlife Medicine, 45*(3), 642–644. https://doi.org/10.1638/2013-0050R2.1
Straight, W. H., Davis, G. L., Skinner, H. C. W., Haims, A., McClennan, B. L., & Tanke, D. H. (2009). Bone lesions in hadrosaurs: computed tomographic imaging as a guide for paleohistologic and stable-isotopic analysis. *Journal of Vertebrate Paleontology, 29*(2), 315–325. https://doi.org/10.1671/039.029.0211
Tanke, D. H., & Rothschild, B. M. (2014). Paleopathology in Late Cretaceous Hadrosauridae from Alberta, Canada with comments on a putative *Tyrannosaurus* bite injury on an *Edmontosaurus* tail. In D. A. Eberth & D. C. Evans (Eds.), *Hadrosaurs*. Indiana University Press.
Waskow, K., & Sander, P. M. (2014). Growth record and histological variation in the dorsal ribs of *Camarasaurus* sp. (Sauropoda). *Journal of Vertebrate Paleontology, 34*(4), 852–869. https://doi.org/10.1080/02724634.2014.840645
Wick, M. R., McDermott, M. B., & Swanson, P. E. (2014). Proliferative, reparative, and reactive benign bone lesions that may be confused diagnostic with true osseous neoplasms. *Seminars in Diagnostic Pathology, 31*(1), 66–88. https://doi.org/10.1053/j.semdp.2013.12.002
Woodward, H. N., Horner, J. R., & Farlow, J. O. (2011). Osteohistological evidence for determinate growth in the American Alligator. *Journal of Herpetology, 45*(3), 339–342. https://doi.org/10.1670/10-274.1
Xing, L., Rothschild, B. M., Randolph-Quinney, P. S., Wang, Y., Parkinson, A. H., & Ran, H. (2018). Possible bite-induced abscess and osteomyelitis in *Lufengosaurus* (Dinosauria: Sauropodomorph) from the Lower Jurassic of the Yimen Basin, *China. Scientific Reports, 8*(1), 5045. https://doi.org/10.1038/s41598-018-23451-x
Zahner, M., & Brinkmann, W. (2019). A Triassic averostran-line theropod from Switzerland and the early evolution of dinosaurs. *Nature Ecology & Evolution, 3*(8), 1146–1152. https://doi.org/10.1038/s41559-019-0941-z

Publisher's Note